Molecular Microbiology (2014) 92(6), 1343–1356 ■
doi:10.1111/mmi.12631
First published online 23 May 2014

Mathematical modelling of arsenic transport, distribution and detoxification processes in yeast

Soheil Rastgou Talemi,[1] Therese Jacobson,[2] Vijay Garla,[3] Clara Navarrete,[2] Annemarie Wagner,[4] Markus J. Tamás[2] and Jörg Schaber[1]***

[1]*Institute for Experimental Internal Medicine, Medical Faculty, Otto-von-Guericke University, Leipziger Str. 44, 39120 Magdeburg, Germany.*
[2]*Department of Chemistry and Molecular Biology, University of Gothenburg, S-405 30 Gothenburg, Sweden.*
[3]*Yale Center for Medical Informatics, Yale University, 300 George Street, Suite 501, New Haven, CT 06520-8009, USA.*
[4]*Department of Applied Physics, Chalmers University of Technology, SE-421 96 Gothenburg, Sweden.*

Summary

Arsenic has a dual role as causative and curative agent of human disease. Therefore, there is considerable interest in elucidating arsenic toxicity and detoxification mechanisms. By an ensemble modelling approach, we identified a best parsimonious mathematical model which recapitulates and predicts intracellular arsenic dynamics for different conditions and mutants, thereby providing novel insights into arsenic toxicity and detoxification mechanisms in yeast, which could partly be confirmed experimentally by dedicated experiments. Specifically, our analyses suggest that: (i) arsenic is mainly protein-bound during short-term (acute) exposure, whereas glutathione-conjugated arsenic dominates during long-term (chronic) exposure, (ii) arsenic is not stably retained, but can leave the vacuole via an export mechanism, and (iii) Fps1 is controlled by Hog1-dependent and Hog1-independent mechanisms during arsenite stress. Our results challenge glutathione depletion as a key mechanism for arsenic toxicity and instead suggest that (iv) increased glutathione biosynthesis protects the proteome against the damaging effects of arsenic and that (v) widespread protein inactivation contributes to the toxicity of this metalloid. Our work in yeast may prove useful to elucidate similar mechanisms in higher eukaryotes and have implications for the use of arsenic in medical therapy.

Accepted 27 April, 2014. For correspondence. *E-mail schaber@med.ovgu.de; Tel. (+49) 391 67 14453; Fax (+49) 391 67 13312; **E-mail markus.tamas@cmb.gu.se; Tel. (+46) 31 786 2548; Fax (+46) 31 786 3910.

Introduction

Arsenic is prevalent in the environment and chronic exposure may cause cardiovascular diseases, neurological disorders, liver injury, and cancers of the skin, bladder, liver and lung. Despite its toxicity, arsenic is currently used in medical therapy as a treatment for acute promyelocytic leukaemia and it might also be applied for other haematological and solid cancers. Given this dual role as causative and curative agent of disease, there is a considerable interest in understanding arsenic toxicity and detoxification mechanisms (Soignet *et al.*, 1998; Dilda and Hogg, 2007; Hughes *et al.*, 2011).

Arsenic can exist in various inorganic and organic forms. For simplicity, we will herein refer to arsenic when the exact form is not known or biologically relevant. In nature, arsenic is mainly present as pentavalent arsenate [AsO_4^{3-} or As^V] and trivalent arsenite [$As(OH)_3$ or As^{III}]. As^V is a phosphate analogue that disturbs energy-generation in cells by inhibiting oxidative phosphorylation. As^{III}, the most toxic form of this metalloid, may bind to and interfere with protein activity, affect the pools of cellular antioxidants, trigger DNA damage and interfere with cytoskeletal functions (Shi *et al.*, 2004; Aposhian and Aposhian, 2006; Kitchin and Wallace, 2008; Wysocki and Tamás, 2010; Hughes *et al.*, 2011).

Several key proteins and mechanisms involved in arsenic toxicity and detoxification have been described in the eukaryotic model organism *Saccharomyces cerevisiae* (budding yeast). In several cases, similar mechanisms exist in higher eukaryotes (Wysocki and Tamás, 2010; Wysocki and Tamás, 2011). As^{III} enters *S. cerevisiae* through the aquaglyceroporin Fps1 and yeast cells lacking this protein (*fps1*Δ) are As^{III} resistant (Wysocki *et al.*, 2001). Since Fps1 is a bidirectional channel, it can also mediate As^{III} efflux when the intracellular concentration exceeds that of the extracellular environment (Maciaszczyk-Dziubinska *et al.*, 2010). The mitogen-activated protein kinase (MAPK) Hog1 is activated by As^{III} (Thorsen *et al.*, 2006) and regulates cell cycle resumption during exposure

(Migdal *et al*., 2008; Diner *et al*., 2011). Activated Hog1 can phosphorylate Fps1 and thereby downregulate Fps1-dependent As^{III} transport (Thorsen *et al*., 2006; Mollapour and Piper, 2007). Consequently, deletion of *HOG1* (*hog1*Δ) reduces Fps1 phosphorylation levels and increases Fps1-dependent As^{III} influx and sensitivity (Thorsen *et al*., 2006). However, whether Hog1-mediated phosphorylation inactivates (or 'closes') Fps1 in response to As^{III} to restrict As^{III} influx and enhance tolerance, remains unknown. As^{III} detoxification in *S. cerevisiae* involves two transport systems: the plasma membrane-localized exporter Acr3 and the vacuolar membrane-localized ABC-transporter Ycf1 (Wysocki *et al*., 1997; Ghosh *et al*., 1999). As^{III}-exposed cells induce expression of the *ACR3* gene, which results in increased As^{III} export and enhanced tolerance (Wysocki *et al*., 1997; 2004). Intracellular As^{III} can be conjugated to the thiol moiety of glutathione (GSH) followed by sequestration of the resulting As^{III}-tri-glutathione complex $As(GS)_3$ into vacuoles catalysed by Ycf1 (Ghosh *et al*., 1999). Cells lacking Acr3 (*acr3*Δ) are highly As^{III} sensitive, whereas cells lacking Ycf1 (*ycf1*Δ) show moderate sensitivity. Cells deficient in both Acr3 and Ycf1 (*acr3*Δ*ycf1*Δ) display an additive hypersensitivity (Wysocki *et al*., 1997; 2001; Ghosh *et al*., 1999).

Besides acting as a chelating agent, GSH also protects cells from metal-induced oxidative damage due to its role in cellular redox control (Wysocki and Tamás, 2010). As^{III} exposed yeast cells strongly increase GSH biosynthesis and accumulate high amounts of cytosolic (Thorsen *et al*., 2007) and extracellular (Thorsen *et al*., 2012) GSH. Both mechanisms serve to decrease intracellular/cytosolic free arsenic levels to enhance tolerance (Thorsen *et al*., 2007; 2012). Consequently, cells devoid of glutathione biosynthesis are As^{III} sensitive (Wysocki *et al*., 2004; Preveral *et al*., 2006; Thorsen *et al*., 2007).

Although much has been learned in recent years about the impact of arsenic on cells and the detoxification strategies used to acquire tolerance, several issues remain unresolved:

- How are transporters involved in As^{III} tolerance regulated during exposure?
- How is arsenic distributed within cells? This question is important to explain toxicity mechanism; yet, accurate measurement of cytosolic, vacuolar, protein-bound, and GSH-conjugated arsenic pools remains challenging.
- How do cells respond to chronic versus acute exposure?
- How efficient is vacuolar sequestration for As^{III} detoxification and tolerance?

In this work, we combined arsenic transport assays in *S. cerevisiae* with mathematical modelling to seek answers to the questions above. Mathematical modelling has been proven to be useful in elucidating molecular mechanisms in yeast, e.g. for signalling (Schaber *et al*., 2006; Behar *et al*., 2008), cell cycle regulation (Csikasz-Nagy *et al*., 2009; Adrover *et al*., 2011) and especially in the HOG signal transduction system (Klipp *et al*., 2005; Schaber *et al*., 2010; 2011; 2012; Petelenz-Kurdziel *et al*., 2013). Modelling enables us to quantify formerly qualitative hypothesis. Moreover, a mathematical model forces the researcher to make hypotheses conceptually rigorous and allows for systematic testing of competing hypothesis, as will be demonstrated.

Our combined molecular and modelling analysis suggests that:

- Fps1 is controlled by Hog1-dependent and Hog1-independent mechanisms during arsenite stress.
- As^{III} efflux through Acr3 quickly saturates upon As^{III} stress.
- Ycf1 protein levels are upregulated in As^{III} hyper-accumulating mutants (*acr3*Δ mutants).
- Protein-bound arsenite is the most abundant species during short-term (acute) exposure, whereas GSH-conjugated arsenic dominates during long-term (chronic) exposure.
- Widespread protein inactivation might contribute to arsenic toxicity.
- Increased GSH biosynthesis may protect the proteome against the damaging effects of arsenic.
- There is an export mechanism for As^{III} out of the vacuole.

Results

Quantifying cellular arsenic levels, model construction and validation

As^{III} uptake and efflux are linked to toxicity and detoxification respectively (Wysocki and Tamás, 2010; Wysocki and Tamás, 2011). To explain how various pathways contribute to intracellular arsenic accumulation, we combined quantitative time-course experiments with mathematical modelling. Yeast cells were first pre-treated with 0.1 mM As^{III} for 24 h, and then exposed to extra 1.0 mM As^{III} for 1 h (*Experimental procedures*). Subsequently, cells were washed and resuspended in As^{III}-free medium. Samples were taken during the whole time-course and intracellular arsenic was determined. In this way, As^{III} influx and efflux was measured in wild type, *ycf1*Δ (defective in vacuolar sequestration), *hog1*Δ (defective in Fps1 closure), *acr3*Δ (defective in export), *acr3*Δ *hog1*Δ (defective in both Fps1 closure and export), *acr3*Δ *ycf1*Δ (defective in both export and vacuolar sequestration), and *gsh1*Δ *PRO2-1* (strongly diminished GSH levels) cells. These strains exhibited distinct As^{III} accumulation profiles (Fig. 1). With a few exceptions, the accumulation profiles corresponded well with

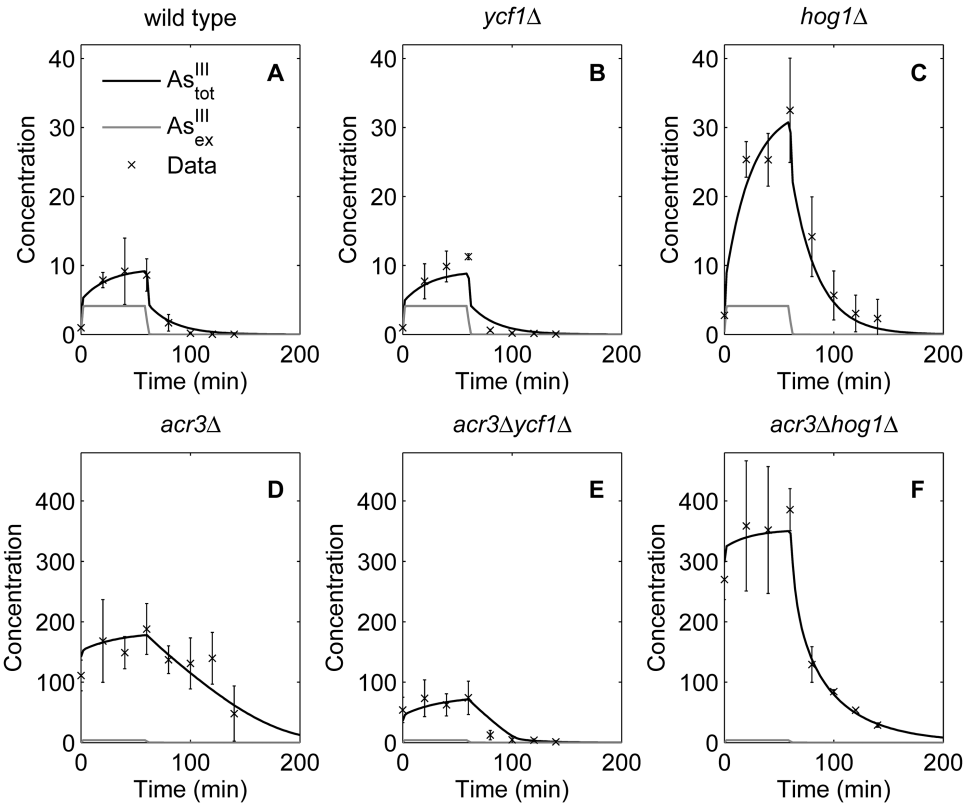

Fig. 1. Comparison of model simulation with arsenic influx–efflux data. Total cellular arsenic (ng per 10^6 cells) versus time (min) is plotted. Solid lines show model simulations and (x) marks show the experimental data [mean ± SD ($n \geq 3$)].
A–F. Comparison between As^{III} influx–efflux data and its simulation for wild type, *ycf1Δ*, *hog1Δ*, *acr3Δ*, *acr3Δ hog1Δ* and *acr3Δ ycf1Δ* using best-ranked model. Plots for *acr3Δ* (D–F) and $ACR3^+$ (A–C) mutants are displayed on the same scale respectively. All data presented here are used for model parameter estimation.

sensitivity of these strains to As^{III} (Supplementary Fig. S1). To assess whether these strains exhibit distinct intracellular distribution profiles we used mathematical models. Model development was guided by the principle of parsimony, i.e. we intended to obtain mathematical models that are as simple as possible and as complex as necessary to both explain the data and address our research questions described above. We implemented an ensemble of parsimonious mathematical models reflecting the uncertainty about the underlying molecular mechanisms of As^{III} transport and intracellular distribution. These models were subsequently trained to explain the data by parameter estimation procedures. We used one part of the data to train the models and estimate the parameters, and another part of the data to validate the models by testing its predictive power using data not used to train the models. We used the measured data for As^{III} uptake and efflux from most mutants, phosphorylated Fps1 and Hog1 phosphorylation/activation data to estimate model parameters (*Supporting information*: Methods). The As^{III} uptake and efflux data from the GSH knock-down strain (*gsh1Δ PRO2-1*) were used for validating the predictive properties of the models (Fig. 4). This seemed reasonable, because one of the goals of this study was to analyse the role of GSH in detoxification. The credibility of results concerning the role of GSH increases, if the models are able to predict a GSH-related experiment, which was not used to train the model. We selected a model which was best supported by the available data and also had good predictive properties (Fig. 2, see *Experimental procedures* for the parameter estimation and model selection procedure). The best model was not only able to reproduce all experimental data well (Figs 1 and 3), but could also well predict the arsenic accumulation profile of GSH knock-down cells (*gsh1Δ PRO2-1*) (Fig. 4). Most of the model parameters (15 out of 20) were practically identifiable (Supplementary Fig. S2) indicating that the parameters are not arbitrary and supporting our intention of developing parsimonious models instead of over-fitted ones. Therefore, we were confident to use the best selected model for further analyses.

The best-ranked model can be found in Biomodels database under identifier MODEL1403280000 (Le Novere *et al.*, 2006).

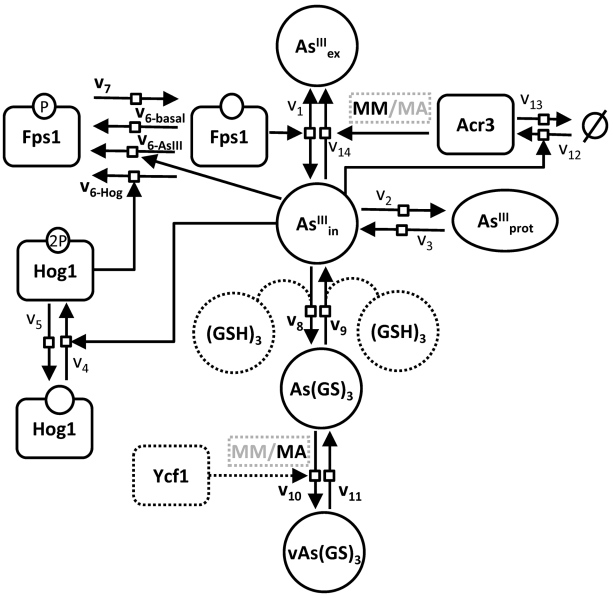

Fig. 2. Alternative model structures. Dotted lines indicate alternative model components implemented in the candidate models. The dark dotted lines indicate alternatives present in the best-ranked model. Four different sources of variation were implemented, each of them able to adopt two different setups, consequently 16 different model combinations were generated: (1) binding of $(GSH)_3$ to As^{III}_{in}/direct conversion of As^{III}_{in} to $As(GS)_3$ through reaction 8 (v_8); (2) Ycf1 concentration is/is not significantly upregulated in *acr3*Δ mutants during pre-incubation in 0.1 mM As^{III}; (3) Michaelis–Menten (MM) or mass action (MA) rate laws for reaction 10 (v_{10}); and (4) MM/MA rate laws for reaction 14 (v_{14}).

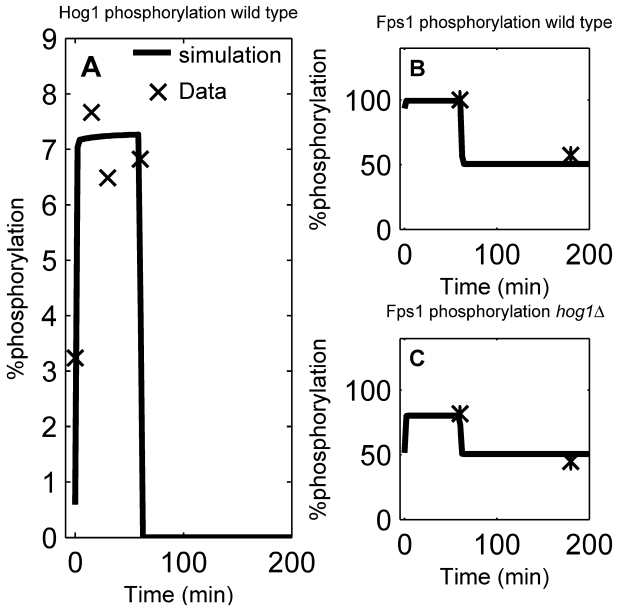

Fig. 3. Comparison of model simulation with cell signalling data. Solid lines show model simulations and (x) marks show the experimental data.
A. Fitted Hog1 phosphorylation (Hog1PP) data by best-ranked model. The Hog1PP percentage in response to As^{III} stress is compared to Hog1PP at 5 min after 0.4M NaCl stress (*Supporting information*: Scaling data). The data are derived from Thorsen *et al.* (2006).
B and C. Fps1 phosphorylation data in wild type and *hog1Δ* mutant fitted by best-ranked model. Fps1-P data [mean ± SD ($n \geq 8$)] is scaled to Fps1-P at 1 h after 1.0 mM As^{III} stress (*Supporting information*: Scaling data).

Activity and regulation of transporters during arsenite exposure

Fps1 is controlled by Hog1-dependent and Hog1-independent mechanisms during arsenite stress. We first used the model to explore regulation of Fps1 phosphorylation during As^{III} exposure. The simulated time-course of phosphorylated Fps1 (Fps1-P) dynamics largely resembled extracellular arsenite (As^{III}_{ex}) dynamics, suggesting that Fps1 activity is regulated during As^{III} exposure (compare Fig. 3B with Fig. 1A). Simulations also indicated a lower level of Fps1-P in *hog1Δ* cells than in wild type cells upon As^{III} exposure by an almost constant amount of about 20% (Fig. 3B and C). Nevertheless, the dynamics of Fps1 phosphorylation upon As^{III} stress was similar in wild type and *hog1*Δ cells. This suggests that Hog1 contributes to Fps1 phosphorylation in wild type cells, whereas in a *hog1*Δ mutant, an arsenic-dependent mechanism compensates for Hog1 loss (Supplementary Fig. S3). Thus, our data best support a model in which Fps1 is controlled by Hog1-dependent and Hog1-independent mechanisms during arsenite stress.

Acr3-mediated arsenite export quickly saturates. Members of the Acr3 family of arsenic transporters are

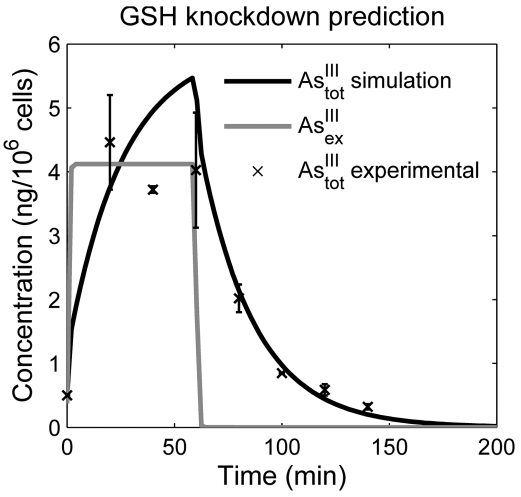

Fig. 4. GSH knock-down experiment and prediction. Solid lines show model simulations and (x) marks show the experimental data [mean ± SD ($n = 4$)]. GSH knock-down mutant (*gsh1Δ PRO2-1*) As^{III} influx–efflux data are excluded from parameter estimation. The best-ranked model can predict the corresponding experiment.

Table 1. Model ranking results.

Rank	Model name	GSH	Ycf1	Vacuole	Export	*n*	*k*	*wSSR*	*AICc*	*AICw*	Cut-off
1st	Model No. 2					64	20	111.09	274.917	0.841	OK
2nd	Model No. 6					64	19	125.18	278.561	0.136	OK
3rd	Model No. 4					64	21	113.1	282.064	0.024	No
4th	Model No. 8					64	20	173.54	303.464	0	No
5th	Model No. 1					64	19	195.34	307.038	0	No
6th	Model No. 5					64	18	223.96	311.788	0	No
7th	Model No. 7					64	19	256.27	324.415	0	No
8th	Model No. 3					64	20	256.68	328.517	0	No
9th	Model No. 13					64	16	545.92	360.813	0	No
10th	Model No. 15					64	17	527.41	362.606	0	No
11th	Model No. 14					64	17	533.31	363.318	0	No
12th	Model No. 12					64	19	475.78	364.012	0	No
13th	Model No. 16					64	18	511.15	364.601	0	No
14th	Model No. 11					64	18	519.86	365.683	0	No
15th	Model No. 9					64	17	624.42	373.412	0	No
16th	Model No. 10					64	18	616.87	376.634	0	No

Variable name				Marker
With GSH binding	Increased Ycf1	MA kinetics for vacuolar sequestration	MA kinetics for As^{III} export trough Acr3	
Without GSH binding	Constant Ycf1	MM kinetics for vacuolar sequestration	MM kinetics for As^{III} export trough Acr3	

Models are ranked according to Akaike Information Criterion corrected for small sample size (*AICc*). GSH knock-down (*gsh1Δ PRO2-1*) influx–efflux data are not used for parameter estimation, but it is used for calculating the objective value (*wSSR*). Top eight models have $(GSH)_3$ binding in their structure and top four models use MM kinetics for As^{III} export through Acr3.
Abbreviations: *n*, number of data points; *k*, number of parameters; *wSSR*, weighted sum of squared residuals; *AICc*, Akaike Information Criterion corrected for small sample size; *AICw*, Akaike weights. MA is Mass Action kinetics and MM is Michaelis–Menten kinetics.

present in every kingdom of life, but their transport properties are not fully characterized. Models containing Michaelis–Menten kinetics for export of free intracellular As^{III} (As^{III}_{in}) ranked first (Table 1), and simulations showed that As^{III}_{in} export via Acr3 is saturated upon 0.1 mM As^{III} exposure with a half-saturation constant of (9.74E-04 μmol l^{-1}) (Supplementary Fig. S4). The corresponding parameter value is very small which turns the As^{III} export practically into a zero-order kinetics. However, the half-saturation constant was not practically identifiable (Supplementary Fig. S2).

Ycf1 levels increase in arsenite hyper-accumulating mutants. The model also provided insight into Ycf1 regulation. The data best support a model in which Ycf1 levels are higher in *acr3Δ* mutants (except in *acr3Δycf1Δ*) than in wild type and other strains (Model No. 2 in Table 1, Ycf1 column). Hence, cells that hyper-accumulate arsenic (see Fig. 1) increase Ycf1 levels, possibly to enhance vacuolar sequestration.

Evidence for a vacuolar export mechanism

We noted that wild type and *ycf1Δ* cells had similar arsenic accumulation profiles (Fig. 1A and B), yet *ycf1Δ* is As^{III} sensitive showing a longer lag phase upon As^{III} stress (Supplementary Fig. S1). We hypothesized that Ycf1-activity is masked by Acr3. Indeed, *acr3Δycf1Δ* mutants accumulated substantially less arsenic than *acr3Δ* (Fig. 1D and E) indicating that vacuolar arsenite ($vAs(GS)_3$) constitutes a significant amount of the total intracellular arsenic pool in *acr3Δ* cells. Model and experimental data show a rapid decrease in intracellular arsenic levels for all strains when cells are resuspended in As^{III}-free medium (Fig. 1). Importantly, albeit with slower kinetics compared to *acr3Δycf1Δ,* the *acr3Δ* mutant can export most intracellular arsenic (Fig. 1D and E) despite a substantial amount being present in the vacuole. Likewise, experimental results show that arsenic export is faster in *acr3Δhog1Δ* than in *acr3Δ* cells (Fig. 1E and F) although the model predicts an even higher amount of vacuolar As^{III} in *acr3Δhog1Δ* than in *acr3Δ* cells (compare Fig. 5F and D). This decrease in

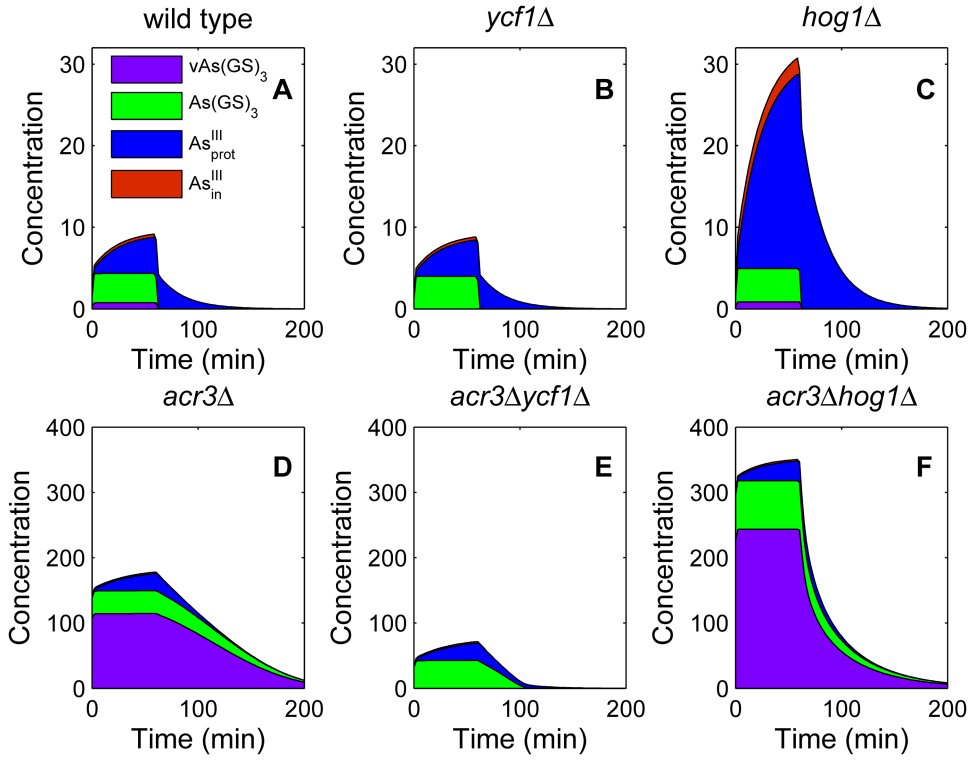

Fig. 5. Intracellular distribution of arsenite species. Intracellular concentration (ng per 10^6 cells) of different As^{III} species is simulated for different mutants during As^{III} uptake and efflux and plotted versus time (min). The area under arsenite simulated influx–efflux curve is divided into its constituents, each representing the contribution of different arsenic species (Area plot).

As^{III}_{tot} cannot be explained by dilution due to cell proliferation as cell numbers stayed constant during the time when arsenic export occurred (Supplementary Fig. S5). Instead, the data support a model in which the decrease in intracellular arsenic in *acr3Δhog1Δ* cells is explained by a mechanism that channels arsenic out of the vacuole.

Proteins are the main target of arsenite during short-term (acute) stress

In situ measurement of intracellular arsenic pools is challenging; yet, the question of how arsenic is distributed within cells is important to explain toxicity mechanism. We therefore used the model to explore subcellular distribution of arsenic in yeast. Interestingly, model simulations suggest that 77%–91% of the increase in As^{III}_{tot} during acute As^{III} exposure (i.e. addition of 1.0 mM As^{III}) is explained by an increase in protein-bound arsenite (As^{III}_{prot}) (Fig. 5). This feature is not only the case for different mutants, but also for different stress regimes as As^{III}_{prot} increased more than other arsenic pools in response to As^{III}_{in} concentrations ranging from 0.5 to 2.0 mM (Supplementary Fig. S6). Hence, the model suggests that proteins are the primary targets for As^{III} under acute exposure. In addition, we conducted a sensitivity analysis of the model parameters by systematically changing each parameter and analysing for its impact on model simulations (see Sensitivity Analysis in *Supporting information*). This sensitivity analysis suggested that protein binding and dissociation reaction rates (k_2 and k_3) are the most important model parameters with respect to total As^{III} level change in wild type cells (*Supporting information*: Sensitivity Analysis, Supplementary Figs S7 and S8).

Glutathione-conjugated arsenite is the most abundant arsenite species during long-term (chronic) stress

Experimental data showed that initial intracellular arsenite concentrations after 24 h of pre-incubation varied between two orders of magnitude, especially for the *acr3Δ* mutants (Fig. 1D–F). In those mutants, As^{III}_{ex} and As^{III}_{in} concentrations equilibrate by passive flux through Fps1 and, thus, are assumed to initially be the same for all these mutants. Consequently, at the initial equilibrium after 24 h of pre-incubation, the protein bound arsenite (As^{III}_{prot}), as a function of free intracellular arsenite (As^{III}_{in}), is also the same for the *acr3Δ* mutants. Thus, the large variation of initial total intracellular arsenic in those mutants can only be accommodated with our model family by varying initial concentrations of GSH-

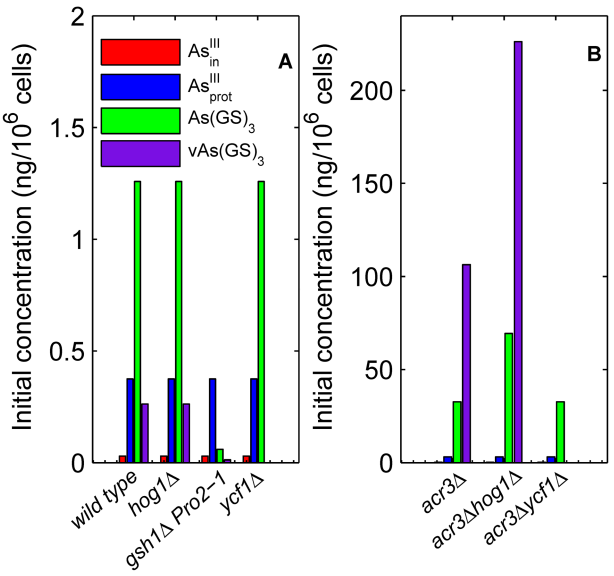

Fig. 6. Concentration of different As^{III} species after chronic exposure.
A. Intracellular concentration (ng per 10^6 cells) of different As^{III} species is simulated for the wild type and mutants having the ACR3 gene ($ACR3^+$ mutants).
B. As^{III} species concentration for *acr3Δ* mutants.

conjugated As^{III} species by different amounts of initial GSH. Accordingly, in the best-ranked model (No. 2) the GSH-conjugated As^{III} species $As(GS)_3$ and $vAs(GS)_3$ are the most abundant As^{III} species after long-term/chronic exposure (i.e. initial concentrations after 24 h pre-incubation with 0.1 mM As^{III}), unless GSH is strongly downregulated (as in *gsh1Δ PRO2-1* cells) (Fig. 6).

Model analysis also suggested that the concentrations of GSH-conjugated As^{III} species saturate as a function of As^{III}_{in} due to limited total amount of GSH, whereas As^{III}_{prot} increases linearly with As^{III}_{in} due to the unlimited protein pool (Supplementary Fig. S10). This also explains why As^{III}_{prot} becomes the most prominent arsenite species after acute stress. However, the concentrations of GSH-conjugated As^{III} species increase linearly with cellular GSH levels (Supplementary Fig. S11). Thus, $As(GS)_3$ should increase as long as GSH is upregulated upon arsenite exposure. To test this idea, we modified the model such that the cellular GSH level continuously increased during As^{III} exposure (*Supporting information*: Modified Model Changes). The modified model simulations showed that GSH upregulation can result in $As(GS)_3$ being the most abundant As^{III} species after 24 h treatment with 1.0 mM As^{III} (Fig. 7). In addition, sensitivity analysis of best-ranked model suggested that As^{III}_{in}-GSH conjugation rates (k_8 and k_9) are the most sensitive model parameter affecting total As^{III} level change in *acr3Δ* cells (Supplementary Figs S7 and S8).

To test the model predictions (GSH upregulation during AsIII exposure and GSH concentration in *acr3Δ* mutants compared to wild type after chronic exposure), we conducted a dedicated experiment. A qualitative assay showed that a 6 h exposure to 0.1 mM As^{III} resulted in higher GSH levels in all strains tested. Moreover, *acr3Δ* mutants produced more GSH than wild type cells and mutants expressing a functional Acr3 (Supplementary Fig. S9). Thus, experimental data confirmed the model predictions.

Taken together, our modelling framework combined with experimental assays suggests that GSH is upregulated during long-term exposure and sequesters most As^{III}_{in} in GSH-conjugated As^{III} species, whereas under acute stress most arsenite binds to protein.

Glutathione protects the proteome against the damaging effects of arsenic

The above model analysis suggested that enhanced GSH biosynthesis may protect the proteome from the damaging effects of arsenic. As^{III} may impact the proteome in two ways: (i) it can bind to proteins thereby interfering with protein activity (Kitchin and Wallace, 2008; Hughes *et al.*, 2011), and (ii) it can disrupt protein function by triggering misfolding and aggregation of newly synthesized proteins (Jacobson *et al.*, 2012). To experimentally address the prediction that GSH protects the proteome against arsenic-induced damage, we moni-

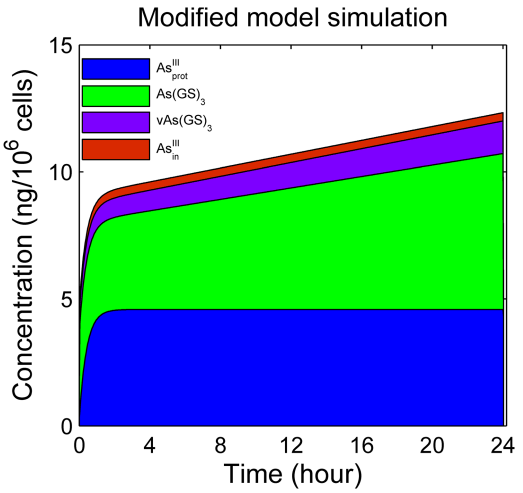

Fig. 7. Simulation of As^{III} species with continuous GSH production. Intracellular concentration (ng per 10^6 cells) of different As^{III} species is simulated for 24 h and wild type cells using a modified model with continuous GSH production, plotted using area plots. GSH conjugation gradually surpasses protein binding in the presence of 1.0 mM of As^{III} during 24 h of simulation. No cell division is considered for the 24 h simulation, which is a reasonable assumption, because of the sensitivity of cells to high As^{III} dose (1.0 mM). Ycf1 level was assumed fix during simulation.

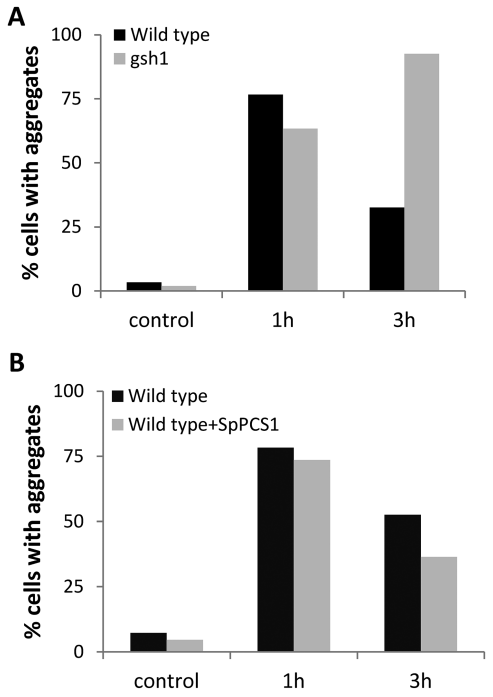

Fig. 8. Quantification of protein aggregation in response to As^{III}. Hsp104–GFP distribution was scored in unexposed (control) cells and during exposure to 0.5 mM As^{III}.
A. Cells deficient in GSH biosynthesis (*gsh1*Δ cells) accumulate more aggregates than wild type cells. The fraction of cells with at least one aggregate/Hsp104–GFP focus was determined at the indicated time points by visual inspection of 100–300 cells.
B. Expression of *PCS1* gene (from *Schizosaccharomyces pombe*) encoding phytochelatin synthase in budding yeast results in less aggregates during exposure to 0.5 mM As^{III}. Wild type yeast was transformed with a plasmid harbouring the *S. pombe PCS1* gene or an empty vector as a control. The transformants were analysed for As^{III} -induced protein aggregation by monitoring Hsp104-GFP distribution as above in 350–580 cells.

tored protein aggregation in living cells by following the subcellular distribution of Hsp104 (a major disaggregating chaperone) coupled to GFP (green fluorescent protein) as marker for aggregate formation. Hsp104–GFP was evenly distributed throughout the cytosol in unexposed cells, whereas As^{III} triggered Hsp104–GFP redistribution to distinct foci that represent sites of protein aggregation (Supplementary Fig. S12) (Jacobson *et al.*, 2012). Quantifying protein aggregation by counting the fraction of cells with Hsp104–GFP foci revealed that about 75% of wild type cells contained aggregates after 1 h of As^{III} exposure (Fig. 8A). After 3 h, most wild type cells had cleared the cytosol from protein aggregates. In contrast, cells defective in GSH biosynthesis (*gsh1*Δ cells) still showed extensive protein aggregation (> 90% of cells contained aggregates) after 3 h of exposure (Fig. 8A). To test whether it is the As^{III} chelating property of GSH that protects the proteome from aggregation, we enabled synthesis of the As^{III}-chelating molecule phytochelatin in S. *cerevisiae* cells that normally do not synthesize this molecule (Clemens *et al.*, 1999; Wysocki *et al.*, 2003). For this, we transformed wild type cells with a plasmid harbouring the *PCS1* gene (from *Schizosaccharomyces pombe*) encoding phytochelatin synthase or an empty vector as a control. Next, we quantified As^{III}-induced protein aggregation of the transformants as described above. Indeed, cells expressing the *PCS1* gene [and hence capable of synthesizing phytochelatin (Wysocki *et al.*, 2003)] had less aggregates than those not expressing *PCS1* (Fig. 8B). Taken together, these experimental results support the model prediction that GSH protects the proteome against the damaging effects of arsenic, probably by chelating this metalloid.

Discussion

In this study, we combined mathematical modelling and experimental data to explore several issues related to arsenite transport, intracellular distribution and detoxification processes in yeast.

Activity and regulation of transporters

The model provided novel understanding of transporter activity and regulation. First, we explored whether Hog1 contributes to Fps1 inactivation ('closure') upon As^{III} stress as a mechanism to restrict As^{III}_{ex} influx and enhance tolerance. The model was able to explain Fps1 phosphorylation, As^{III} influx–efflux and Hog1 phosphorylation data. The dynamics of Fps1 phosphorylation shows a significant analogy to As^{III}_{ex} dynamics, suggesting a quick response (i.e. 'closure') of Fps1 that may result in enhanced tolerance. The model suggested that Hog1 is the main Fps1 regulator, but that in the absence of Hog1 (*hog1*Δ cells) another arsenic-dependent mechanism can regulate Fps1 phosphorylation/activity. Moreover, sensitivity analysis of Fps1 phosphorylation suggested that the dephosphorylation reaction rate (k_7) is the most sensitive model parameter affecting Fps1-P level change during As^{III} exposure and after cell wash for both wild type and *acr3*Δ cells (Supplementary Figs S13 and S14), suggesting that dephosphorylation plays an important role in Fps1 regulation. Identification of the kinase(s) and phosphatase(s) involved in Fps1 phosphorylation and dephosphorylation will be important to further elucidate how cells limit arsenic influx and toxicity. The identifiability analysis supported the calibration of Fps1 phosphorylation parameters (Supplementary Fig. S2).

Second, the model suggested a quickly saturating Michaelis–Menten kinetics for As^{III} export via Acr3. This finding is supported by the recent demonstration that Acr3 is an arsenite/proton antiporter characterized by Michaelis–Menten-type saturation kinetics (Maciaszczyk-

Dziubinska *et al*., 2011) and adds to our understanding of the transport properties of this widespread family of arsenite exporters.

Third, the best-ranked model had higher Ycf1 levels in cells lacking Acr3 (except for *acr3Δycf1Δ*) than in cells expressing Acr3. This model prediction is in agreement with experimental data showing that expression of the *YCF1* gene is hyper-induced in mutants with elevated As^{III}_{in} concentrations (Wysocki *et al*., 2004). Under the same experimental conditions, *YCF1* expression is not induced by arsenic in wild type cells (Wysocki *et al*., 2004). These experimental data further support the model.

Evidence of a vacuolar arsenic export mechanism

The relevance of vacuolar sequestration of metal-glutathione conjugates as a detoxification mechanism in yeast is inferred from the metal sensitivity of mutants defective in this process (reviewed in Wysocki and Tamás, 2010). It has been postulated that vacuolar sequestration of $As(GS)_3$ is particularly relevant for arsenic detoxification given that the vacuole is acidic and that the $As(GS)_3$ complex is more stable at low pH *in vitro* (Canovas *et al*., 2004; Rey *et al*., 2004). Yet, deletion of *YCF1* (*ycf1Δ*) only caused moderate As^{III} sensitivity, visible as a longer lag phase while the growth rate is unaffected (Supplementary Fig. S1). Moreover, *YCF1* gene expression is not induced in wild type cells during As^{III} exposure (Wysocki *et al*., 2004). Hence, the relative importance of this pathway for As^{III} detoxification remains unclear. Here, we provide evidence that As^{III} is not stably retained in the vacuole; *acr3Δ* and *acr3Δhog1Δ* cells diminished intracellular arsenic despite having a significant fraction of the total cellular arsenic present in the vacuole (Figs 1 and 5D–F). How does vacuolar As^{III} leave yeast cells? Vacuolar As^{III} could be exported via exocytosis or it could first enter the cytosol and then be exported out of cells. It has been shown that Fps1 can mediate As^{III} efflux when the intracellular concentration exceeds that of the extracellular environment (Maciaszczyk-Dziubinska *et al*., 2010). Moreover, deletion of *HOG1* increases Fps1-mediated As^{III} transport (Thorsen *et al*., 2006). Assuming that most As^{III} leaves *acr3Δhog1Δ* cells through hyper-activated Fps1 (Maciaszczyk-Dziubinska *et al*., 2010) argues that vacuolar As^{III} first enters the cytoplasm for subsequent export rather than leaving cells via exocytosis. The finding that $As(GS)_3$ is not well retained in the vacuole is unexpected given that vacuolar sequestration of glutathione-conjugates is a conserved detoxification mechanism in yeasts and plants (reviewed in Wysocki and Tamás, 2010). Nevertheless, vacuolar degradation of glutathione-conjugates via γ-glutamyl-transpeptidase activity has been described in *Arabidopsis* (Grzam *et al*., 2007; Ohkama-Ohtsu *et al*., 2007), and a similar degradation pathway appears to exist in yeast (Ubiyvovk *et al*., 2006; Wunschmann *et al*., 2010). Whether this pathway is responsible for $As(GS)_3$ catabolism is currently unknown. The protein responsible for vacuolar arsenic export and the form of arsenic that this protein recognizes is not known. Assuming that *acr3Δhog1Δ* cells export arsenic through hyper-active Fps1, it is possible that arsenic enters the cytosol from the vacuole as $As(OH)_3$, which is the form recognized by Fps1. Interestingly, *S. cerevisiae* possesses an uncharacterized Fps1 homologue encoded by the *YFL054c* gene. Whether Yfl054c is localized to the vacuolar membrane and mediates vacuolar arsenic export remains to be investigated.

What is the role of Ycf1 for detoxification?

If arsenic is not stably retained in the vacuole, what is then the importance of Ycf1-mediated sequestration of $As(GS)_3$? The vacuole probably contributes to arsenite tolerance by keeping the As^{III}_{in} steady-state concentration below a certain (critical) level, exemplified by a higher As^{III} sensitivity of *acr3Δycf1Δ* compared to *acr3Δ* (Supplementary Fig. S1). We previously speculated that conjugation of As^{III} to GSH is rate-limiting and that a basal level of Ycf1 in the vacuolar membrane is sufficient for tolerance (Wysocki *et al*., 2004). Supporting this hypothesis, simulations suggested that vacuolar arsenite ($vAs(GS)_3$) increases along with $As(GS)_3$ increase (Fig. 7). This hypothesis also explains why overexpression of *YCF1* (driven by the strong *GAL1* promoter) does not improve As^{III} resistance of yeast (Preveral *et al*., 2006). The steady-state concentration of As^{III}_{in} and consequently As^{III}_{prot} is independent of $vAs(GS)_3$ in the best-ranked model. This is due to a simplified version of the $(GSH)_3$ conjugation mechanism used here (*Supporting information*: Steady-state calculations). Hence, to better understand the contribution of the vacuole in tolerance acquisition, we need to quantify and include As^{III} induced GSH, Ycf1 and Acr3 upregulation mechanisms.

Protein-binding and glutathione-conjugation of arsenite during acute and chronic arsenite exposure

Model simulations suggested that 77%–91% of the increase in As^{III}_{tot} during acute As^{III} exposure (i.e. addition of 1.0 mM As^{III}) is explained by an increase in protein-bound arsenite (As^{III}_{prot}) in wild type cells and all mutants (Fig. 5). In addition, sensitivity analysis of the best-ranked model suggested that k_2 (As^{III}_{in}–protein association rate constant) and k_3 (As^{III}_{in}–protein dissociation rate constant) are the most sensitive model parameters affecting cellular arsenic levels during As^{III} exposure and after cell wash in wild type. Hence, the sensitivity analysis emphasizes that proteins are the main targets of As^{III} in wild type cells during acute

As^{III} exposure. Since arsenic-binding can inhibit protein activity (Kitchin and Wallace, 2008; Hughes *et al.*, 2011), our model suggests that widespread protein inactivation may be a major toxicity mechanism. Moreover, we recently demonstrated that As^{III} disrupts protein function and causes toxicity by triggering misfolding and aggregation of newly synthesized proteins (Jacobson *et al.*, 2012). Thus, As^{III} inhibits protein activity in two ways; by direct binding to folded proteins and by interfering with folding of nascent polypeptides. This work also provided insight into the dynamics of subcellular arsenic distribution. GSH plays an important role in As^{III} detoxification and tolerance, and GSH biosynthesis is stimulated during As^{III} exposure (Thorsen *et al.*, 2007). For the sake of simplicity, we assumed that cellular GSH content does not increase during 1 h of As^{III} stress; however, we included the possibility of higher initial GSH levels for *acr3*Δ mutants in some models. Including this possibility was reasonable given the observed hyperactivation of Yap1 in mutants with elevated intracellular As^{III} and that Yap1 controls expression of GSH biosynthesis genes (Wysocki *et al.*, 2004; Thorsen *et al.*, 2007). These models, in fact, were ranked best, because only they could accommodate large variations in initial intracellular arsenic concentrations in *acr3*Δ mutants. This prediction was experimentally confirmed (Supplementary Fig. S9). The model predicted higher concentration of GSH-conjugated than protein bound As^{III} species after 24 h As^{III} exposure (pre-incubation), except when GSH production is down-regulated (i.e. in *gsh1*Δ *PRO2-1* cells) (Fig. 6). This finding suggests that enhanced GSH biosynthesis may protect the proteome from the damaging effects of As^{III}. In support of this prediction, we experimentally demonstrated that GSH biosynthesis-deficient cells accumulated more aggregated/damaged proteins than wild type cells, whereas cells with increased As^{III}-chelating capacity showed decreased levels of aggregated/damaged proteins (Fig. 8).

Correlation between intracellular arsenic distribution and toxicity

Correlating the predicted distribution of intracellular arsenic and the As^{III}-sensitivity of different mutants can expand our understanding of arsenic toxicity mechanisms. Our results indicate that cells with a higher proportion of protein-bound arsenic (*hog1*Δ, *acr3*Δ, *acr3*Δ*hog1*Δ, *acr3*Δ*ycf1*Δ) are more arsenite sensitive (Supplementary Fig. S1) (also Thorsen *et al.*, 2006), supporting the notion that widespread protein inactivation contributes to the toxicity of this metalloid. In contrast, our results do not show a direct correlation between increased GSH conjugation and As^{III} sensitivity (growth and simulation of As^{III}_{in} in *acr3*Δ and *acr3*Δ*ycf1*Δ cells in Supplementary Figs S1 and S5). This result challenges GSH depletion as a major arsenic toxicity mechanism in yeast. Curiously, the GSH knock-down strain is not very As^{III} sensitive despite most of the intracellular arsenic appears protein-bound (Supplementary Fig. S1). However, the total amount of intracellular arsenic is lower in this strain than in the corresponding wild type (compare Fig. 1A with Fig. 4). Hence, *gsh1*Δ*PRO2-1* cells might compensate for the lack of GSH with other (unknown) tolerance mechanisms.

To conclude, we selected a model out of an ensemble of designed models, which represented simplified mechanisms of As^{III} accumulation in yeast cells. This simplified model has been instrumental to provide novel insights into several aspects of arsenic transport, intracellular distribution and detoxification processes, which could partly be confirmed experimentally. Because arsenic toxicity and detoxification mechanisms appear conserved in various eukaryotes, this work in yeast may prove useful to elucidate similar mechanisms in other organisms and have implications for the use of arsenic in medical therapy.

Experimental procedures

Experimental strains and growth conditions

The *S. cerevisiae* strains and plasmids used in this study are described in Supplementary Table S1. Yeast strains were grown at 30°C in minimal synthetic complete (SC) medium (0.67% yeast nitrogen base) and 2% glucose as a carbon source. Sodium arsenite (NaAsO2) was obtained from Sigma-Aldrich.

Determination of intracellular arsenic during influx–efflux

Intracellular arsenic was measured essentially as described previously (Thorsen *et al.*, 2006). Briefly, cells were first exposed to 0.1 mM As^{III} for ~ 24 h (chronic exposure) before addition of 1.0 mM As^{III} (acute exposure). The pre-exposure is required to correctly assess the contribution of Acr3 to As^{III} efflux (Ghosh *et al.*, 1999; Thorsen *et al.*, 2006). Cultures were incubated for 1 h with 1.0 mM As^{III} to allow intracellular accumulation, then washed and resuspended in As^{III}-free medium to allow As^{III} efflux. Cells were collected at the indicated time points, washed in ice-cold water and pelleted by centrifugation. Cell pellets were resuspended in water, boiled for 10 min, centrifuged, and the supernatants were collected. The arsenic content of each sample was determined using a graphite furnace atomic absorption spectrometer (SIMAA 6000; Perkin-Elmer) as described previously (Wagner and Boman, 2004). Arsenic influx–efflux measurements were performed at least twice from independent cell cultures.

Microscopy

Yeast cells expressing Hsp104-GFP were grown to mid-log phase in SC medium containing appropriate amino acid requirements for plasmid selection or in rich YPD (1% yeast extract, 2% peptone, and 2% glucose) medium. To induce

PCS1 expression, 2% galactose was used. Cells were washed twice with water or PBS and the GFP signals were observed in living cells using a Leica DM RXA (Leica Microsystems) fluorescence microscope equipped with 100× HCX PL Fluotar 1.30 objective and appropriate fluorescence light filter sets. Images were captured with digital camera [Hamatasu C4742-95 (Hamamatasu Photonics)] and QFluoro software, and processed with Photoshop CS (Adobe Systems). To quantify protein aggregation we use several images taken from the same culture and also from independent cultures. In each image we count the total number of cells and the number of cells that contain HSP104-GFP foci to calculate the fraction of cells that show Hsp104-GFP foci. For each condition/mutant, we count several hundreds of cells by visual inspection.

Data processing

Experimental data were scaled in various ways to be comparable to the model simulations (*Supporting information*: Scaling Data).

Model formulation

In order to model processes that are relevant for As^{III} toxicity and detoxification in yeast, 16 different mathematical models were implemented as ordinary differential equations (ODEs). The models are highly simplified representations of the biochemical network underlying As^{III}-mediated signalling, complex formation and influx–efflux. The mathematical formulation of the described processes and all estimated parameters and initial conditions are detailed in the Supplementary Tables S2–S6, whose structure is explained in *Supporting information*: Models Setup Summary. For simplicity and for the lack of appropriate data, mass action kinetics was used in most reactions. Following the principle of parsimony for model development, only state variables that we felt were absolutely necessary was included in the model and all processes were reduced to a minimum. Still, there are processes and state variables where it was not obvious, whether they would be necessary or not to explain the data. Those we subjected to a systematical model selection analysis detailed below. We now separately address the main variables and processes considered in detail. Reactions numbers refer to Fig. 2.

Fps1-mediated arsenite influx, protein binding

As^{III} influx–efflux through Fps1 was considered as a passive diffusion process (Reaction v_1 in Fig. 2) regulated by the phosphorylation state of Fps1. The phosphorylated form of Fps1 (Fps1-P) is considered as the inactive/closed state of the channel (Thorsen *et al.*, 2006). Both binding and dissociation of As^{III} to/from proteins was implemented using mass action kinetics (reactions v_2 and v_3). Protein-bound arsenite (As^{III}_{prot}) is not available for sequestration to the vacuole or efflux via Fps1 or Acr3.

Hog1 and Fps1 regulation

The MAPK Hog1 becomes dually phosphorylated and, thereby, activated in response to As^{III} exposure (Thorsen *et al.*, 2006), which is considered here as a single constitutive reaction (Reaction v_4). Hog1 dephosphorylation is also implemented as a single reaction (Reaction v_5). Due to the uncertainty about the Fps1 regulation mechanisms, we distinguished three different Fps1 phosphorylation mechanisms within the model. First, basal Fps1 phosphorylation, which is independent of As^{III} stress (Reaction v_{6_basal} in Fig. 2). Second, Hog1-dependent Fps1 phosphorylation (Reaction v_{6_Hog1PP} in Fig. 2). Third, As^{III}_{in}-dependent Fps1 phosphorylation (Reaction $v_{6\_As^{III}}$ in Fig. 2). Fps1 dephosphorylation was also assumed as mass action kinetics (Reaction v_7). Fps1 and Hog1 phosphorylation data are detailed in Supplementary Table S7.

Arsenite-glutathione conjugation

As^{III}_{in} can conjugate with three GSH molecules to form $As(GS)_3$ (Delnomdedieu *et al.*, 1994). For simplicity, we introduced the species $(GSH)_3$, which represents three GSH molecules and we can use a simple rate law for As^{III}_{in}-GSH conjugation. As^{III}_{in}-GSH conjugation was implemented in two different ways in reaction v_8 (Fig. 2): first, As^{III}_{in} directly converts to $As(GS)_3$ (Fig. 2), i.e. independent of the GSH concentration. Such a mechanisms would disregard possible effects of GSH depletion or upregulation; second, we explicitly consider a binding reaction of $(GSH)_3$ to As^{III}_{in}. Such a formulation allows considering effects of GSH depletion (or rather saturation of $As(GS)_3$ formation), as well as different initial $As(GS)_3$ values through different initial $(GSH)_3$ values and corresponding steady-state concentration.

We allowed for three different initial $(GSH)_3$ concentrations, depending on the considered mutant:

(1) $(GSH)_{3\text{-wt-}0}$: was used for wild type and *ycf1*Δ and *hog1*Δ mutants
(2) $(GSH)_{3\text{-}acr3\Delta\text{-}0}$: was used for *acr3*Δ and *acr3*Δ*ycf1*Δ mutants
(3) $(GSH)_{3\text{-}acr3\Delta hog1\Delta\text{-}0}$: was used for *acr3*Δ*hog1*Δ mutant.

$(GSH)_{3\text{-wt-}0}$ is equal to cellular GSH level in Muller (1996) and the other $(GSH)_3$ initial concentrations were estimated from experimental data (Supplementary Table S4). No $(GSH)_3$ production or degradation reaction was considered in the models, assuming that cellular GSH content is not significantly altered during 1 h incubation with high As^{III} concentration. $As(GS)_3$ dissociation is considered as mass action kinetics (Reaction v_9).

Ycf1-mediated vacuolar sequestration

Experimental data indicate that *YCF1* gene expression is not significantly upregulated in response to As^{III} exposure (Wysocki *et al.*, 2004; Thorsen *et al.*, 2007), except in cells that hyperaccumulate As^{III}, i.e. in *acr3*Δ mutants (Wysocki *et al.*, 2004). Based on this information, two alternative setups were considered in *acr3*Δ mutants (except *acr3*Δ*ycf1*Δ mutant) with same or different Ycf1 level comparing to wild type (Supplementary Table S4 and Models Setup Summary). In all of these models, the Ycf1 level is supposed to be constant during 1 h of 1.0 mM As^{III} stress. In both cases, mass action and Michaelis–Menten kinetics were used alternatively for

vacuolar sequestration of $As(GS)_3$ and lead to 4 different combinations of v_{10} reaction ($v_{10\text{-}a}$,$v_{10\text{-}b}$,$v_{10\text{-}c}$,$v_{10\text{-}d}$) which are detailed in Supplementary Table S3. To design the model such that it starts in steady state, we assumed an efflux process for $vAs(GS)_3$ out of vacuole (Reaction v_{11}), which, however, can become negligible depending on the estimated parameters.

ACR3 transcription and Acr3-mediated arsenite efflux

Due to the lack of experimental data on Acr3 concentrations in the cell, we combined *ACR3* translation and transcription in a single reaction (Reaction v_{12} in Fig. 2). Acr3 is constitutively degraded through reaction v_{13} (Fig. 2). Acr3-mediated As^{III}_{in} export was implemented in reaction v_{14} in two different forms, using either mass action (MA) or Michaelis–Menten (MM) kinetics (Fig. 2).

Initial value of free intracellular arsenite

We assumed that cells reach a steady state during 24 h of pre-incubation with 0.1 mM As^{III}. We suppose that the concentration of intracellular arsenite (As^{III}_{in}) equals As^{III} concentration in the medium (As^{III}_{ex}) in *acr3Δ* mutants. This is based on the assumption that diffusion through Fps1 channel is passive and merely concentration gradient-dependent and that Fps1 is the only As^{III} influx–efflux pathway in *acr3Δ* mutants (Wysocki *et al*., 2001; Liu *et al*., 2004; Maciaszczyk-Dziubinska *et al*., 2010). For wild type cells and all $ACR3^{+}$ mutants, the same initial intracellular arsenite (As^{III}_{in}) was considered, which was estimated from experimental data. These different model setups are depicted (Fig. 2) and outlined (*Supporting information*: Models Setup Summary).

Computational tools and analysis methods

We estimated model parameters from experimental data using COPASI (Hoops *et al*., 2006) and ranked them according to Akaike Information Criterion (*AIC*) using *ModelMage* (Schaber *et al*., 2011) (*Supporting information*: Methods). To calculate the *AIC* we used the weighted sum of squared residuals (*wSSR*) of both the fitted data (Figs 1 and 3) and the predicted data (Fig. 4). This way, we included both the explanatory and the predictive properties of the models in the ranking. The best-ranked model (Fig. 2) was able to predict the GSH knock down strain (*gsh1Δ PRO2-1*) data well (Fig. 4). We conducted a Profile Likelihood-based identifiability analysis (Raue *et al*., 2009; Schaber and Klipp, 2011) using COPASI (Schaber, 2012) (*Supporting information*: Methods). Most parameters (12 out of 20) were practically identifiable (Supplementary Fig. S2). There was only one structurally non-identifiable parameter ($vmax_{14}$), which was previously determined by a preliminary identifiability analysis and set to 1.0. Later, we conducted a local sensitivity analysis for the best approximating model (No. 2) to identify how the concentration of Fps1-P and cellular arsenic level change at the end of simulation with respect to local parameters change, using COPASI (*Supporting information*: Methods). The best-ranked model can be found in Biomodels database under identifier MODEL1403280000 (Le Novere *et al*., 2006).

Acknowledgements

We thank Jean Labarre (CEA-Saclay) and Stefan Hohmann (Gothenburg) for providing yeast strains. M.J.T. was supported by the Swedish Research Council (Grant No. 621-2007-5470). S.R.T. was supported by the Ministry of Education of Saxony-Anhalt (Research Centre Dynamic Systems: Biosystems Engineering) (XD3639HP/0306 and CDS, MW- 21LMS 5) and the International Max Planck Research School (IMPRS) Magdeburg for Advanced Methods in Process and Systems Engineering.

References

Adrover, M.A., Zi, Z., Duch, A., Schaber, J., Gonzalez-Novo, A., Jimenez, J., *et al*. (2011) Time-dependent quantitative multicomponent control of the G(1)-S network by the stress-activated protein kinase Hog1 upon osmostress. *Sci Signal* **4:** ra63.

Aposhian, H.V., and Aposhian, M.M. (2006) Arsenic toxicology: five questions. *Chem Res Toxicol* **19:** 1–15.

Behar, M., Hao, N., Dohlman, H.G., and Elston, T.C. (2008) Dose-to-duration encoding and signaling beyond saturation in intracellular signaling networks. *PLoS Comput Biol* **4:** e1000197.

Canovas, D., Vooijs, R., Schat, H., and de Lorenzo, V. (2004) The role of thiol species in the hypertolerance of *Aspergillus* sp. P37 to arsenic. *J Biol Chem* **279:** 51234–51240.

Clemens, S., Kim, E.J., Neumann, D., and Schroeder, J.I. (1999) Tolerance to toxic metals by a gene family of phytochelatin synthases from plants and yeast. *EMBO J* **18:** 3325–3333.

Csikasz-Nagy, A., Kapuy, O., Toth, A., Pal, C., Jensen, L.J., Uhlmann, F., *et al*. (2009) Cell cycle regulation by feed-forward loops coupling transcription and phosphorylation. *Mol Syst Biol* **5:** 236.

Delnomdedieu, M., Basti, M.M., Styblo, M., Otvos, J.D., and Thomas, D.J. (1994) Complexation of arsenic species in rabbit erythrocytes. *Chem Res Toxicol* **7:** 621–627.

Dilda, P.J., and Hogg, P.J. (2007) Arsenical-based cancer drugs. *Cancer Treat Rev* **33:** 542–564.

Diner, P., Veide Vilg, J., Kjellen, J., Migdal, I., Andersson, T., Gebbia, M., *et al*. (2011) Design, synthesis, and characterization of a highly effective Hog1 inhibitor: a powerful tool for analyzing MAP kinase signaling in yeast. *PLoS ONE* **6:** e20012.

Ghosh, M., Shen, J., and Rosen, B.P. (1999) Pathways of As(III) detoxification in *Saccharomyces cerevisiae*. *Proc Natl Acad Sci USA* **96:** 5001–5006.

Grzam, A., Martin, M.N., Hell, R., and Meyer, A.J. (2007) gamma-Glutamyl transpeptidase GGT4 initiates vacuolar degradation of glutathione S-conjugates in Arabidopsis. *FEBS Lett* **581:** 3131–3138.

Hoops, S., Sahle, S., Gauges, R., Lee, C., Pahle, J., Simus, N., *et al*. (2006) COPASI – a COmplex PAthway SImulator. *Bioinformatics* **22:** 3067–3074.

Hughes, M.F., Beck, B.D., Chen, Y., Lewis, A.S., and Thomas, D.J. (2011) Arsenic exposure and toxicology: a historical perspective. *Toxicol Sci* **123:** 305–332.

Jacobson, T., Navarrete, C., Sharma, S.K., Sideri, T.C., Ibstedt, S., Priya, S., *et al*. (2012) Arsenite interferes with

protein folding and triggers formation of protein aggregates in yeast. *J Cell Sci* **125:** 5073–5083.
Kitchin, K.T., and Wallace, K. (2008) The role of protein binding of trivalent arsenicals in arsenic carcinogenesis and toxicity. *J Inorg Biochem* **102:** 532–539.
Klipp, E., Nordlander, B., Kruger, R., Gennemark, P., and Hohmann, S. (2005) Integrative model of the response of yeast to osmotic shock. *Nat Biotechnol* **23:** 975–982.
Le Novere, N., Bornstein, B., Broicher, A., Courtot, M., Donizelli, M., Dharuri, H., *et al*. (2006) BioModels Database: a free, centralized database of curated, published, quantitative kinetic models of biochemical and cellular systems. *Nucleic Acids Res* **34:** D689–D691.
Liu, Z., Boles, E., and Rosen, B.P. (2004) Arsenic trioxide uptake by hexose permeases in *Saccharomyces cerevisiae*. *J Biol Chem* **279:** 17312–17318.
Maciaszczyk-Dziubinska, E., Migdal, I., Migocka, M., Bocer, T., and Wysocki, R. (2010) The yeast aquaglyceroporin Fps1p is a bidirectional arsenite channel. *FEBS Lett* **584:** 726–732.
Maciaszczyk-Dziubinska, E., Migocka, M., and Wysocki, R. (2011) Acr3p is a plasma membrane antiporter that catalyzes As(III)/H(+) and Sb(III)/H(+) exchange in *Saccharomyces cerevisiae*. *Biochim Biophys Acta* **1808:** 1855–1859.
Migdal, I., Ilina, Y., Tamás, M.J., and Wysocki, R. (2008) Mitogen-activated protein kinase Hog1 mediates adaptation to G1 checkpoint arrest during arsenite and hyperosmotic stress. *Eukaryot Cell* **7:** 1309–1317.
Mollapour, M., and Piper, P.W. (2007) Hog1 mitogen-activated protein kinase phosphorylation targets the yeast Fps1 aquaglyceroporin for endocytosis, thereby rendering cells resistant to acetic acid. *Mol Cell Biol* **27:** 6446–6456.
Muller, E.G. (1996) A glutathione reductase mutant of yeast accumulates high levels of oxidized glutathione and requires thioredoxin for growth. *Mol Biol Cell* **7:** 1805–1813.
Ohkama-Ohtsu, N., Zhao, P., Xiang, C., and Oliver, D.J. (2007) Glutathione conjugates in the vacuole are degraded by γ-glutamyl transpeptidase GGT3 in Arabidopsis. *Plant J* **49:** 878–888.
Petelenz-Kurdziel, E., Kuehn, C., Nordlander, B., Klein, D., Hong, K.-K., Jacobson, T., *et al*. (2013) Quantitative analysis of glycerol accumulation, glycolysis and growth under hyper osmotic stress. *PLoS Comput Biol* **9:** e1003084.
Preveral, S., Ansoborlo, E., Mari, S., Vavasseur, A., and Forestier, C. (2006) Metal(loid)s and radionuclides cytotoxicity in *Saccharomyces cerevisiae*. Role of YCF1, glutathione and effect of buthionine sulfoximine. *Biochimie* **88:** 1651–1663.
Raue, A., Kreutz, C., Maiwald, T., Bachmann, J., Schilling, M., Klingmuller, U., and Timmer, J. (2009) Structural and practical identifiability analysis of partially observed dynamical models by exploiting the profile likelihood. *Bioinformatics* **25:** 1923–1929.
Rey, N.A., Howarth, O.W., and Pereira-Maia, E.C. (2004) Equilibrium characterization of the As(III)-cysteine and the As(III)-glutathione systems in aqueous solution. *J Inorg Biochem* **98:** 1151–1159.
Schaber, J. (2012) Easy parameter identifiability analysis with COPASI. *Biosystems* **110:** 183–185.
Schaber, J., and Klipp, E. (2011) Model-based inference of biochemical parameters and dynamic properties of microbial signal transduction networks. *Curr Opin Biotechnol* **22:** 109–116.
Schaber, J., Kofahl, B., Kowald, A., and Klipp, E. (2006) A modelling approach to quantify dynamic crosstalk between the pheromone and the starvation pathway in baker's yeast. *FEBS J* **273:** 3520–3533.
Schaber, J., Adrover, M.A., Eriksson, E., Pelet, S., Petelenz-Kurdziel, E., Klein, D., *et al*. (2010) Biophysical properties of *Saccharomyces cerevisiae* and their relationship with HOG pathway activation. *Eur Biophys J* **39:** 1547–1556.
Schaber, J., Flottmann, M., Li, J., Tiger, C.F., Hohmann, S., and Klipp, E. (2011) Automated ensemble modeling with modelMaGe: analyzing feedback mechanisms in the Sho1 branch of the HOG pathway. *PLoS ONE* **6:** e14791.
Schaber, J., Baltanas, R., Bush, A., Klipp, E., and Colman-Lerner, A. (2012) Modelling reveals novel roles of two parallel signalling pathways and homeostatic feedbacks in yeast. *Mol Syst Biol* **8:** 622.
Shi, H., Shi, X., and Liu, K.J. (2004) Oxidative mechanism of arsenic toxicity and carcinogenesis. *Mol Cell Biochem* **255:** 67–78.
Soignet, S.L., Maslak, P., Wang, Z.G., Jhanwar, S., Calleja, E., Dardashti, L.J., *et al*. (1998) Complete remission after treatment of acute promyelocytic leukemia with arsenic trioxide. *N Engl J Med* **339:** 1341–1348.
Thorsen, M., Di, Y., Tangemo, C., Morillas, M., Ahmadpour, D., Van der Does, C., *et al*. (2006) The MAPK Hog1p modulates Fps1p-dependent arsenite uptake and tolerance in yeast. *Mol Biol Cell* **17:** 4400–4410.
Thorsen, M., Lagniel, G., Kristiansson, E., Junot, C., Nerman, O., Labarre, J., and Tamás, M.J. (2007) Quantitative transcriptome, proteome, and sulfur metabolite profiling of the *Saccharomyces cerevisiae* response to arsenite. *Physiol Genomics* **30:** 35–43.
Thorsen, M., Jacobson, T., Vooijs, R., Navarrete, C., Bliek, T., Schat, H., and Tamás, M.J. (2012) Glutathione serves an extracellular defence function to decrease arsenite accumulation and toxicity in yeast. *Mol Microbiol* **84:** 1177–1188.
Ubiyvovk, V.M., Blazhenko, O.V., Gigot, D., Penninckx, M., and Sibirny, A.A. (2006) Role of gamma-glutamyltranspeptidase in detoxification of xenobiotics in the yeasts *Hansenula polymorpha* and *Saccharomyces cerevisiae*. *Cell Biol Int* **30:** 665–671.
Wagner, A., and Boman, J. (2004) Biomonitoring of trace elements in Vietnamese freshwater mussels. *Spectrochim Acta B At Spectrosc* **59:** 1125–1132.
Wunschmann, J., Krajewski, M., Letzel, T., Huber, E.M., Ehrmann, A., Grill, E., and Lendzian, K.J. (2010) Dissection of glutathione conjugate turnover in yeast. *Phytochemistry* **71:** 54–61.
Wysocki, R., and Tamás, M.J. (2011) *Saccharomyces cerevisiae* as a model organism for elucidating arsenic tolerance mechanisms. In *Cellular Effects of Heavy Metals*. Bánfalvi, G. (ed.). Heidelberg: Springer Verlag Germany, pp. 87–112.
Wysocki, R., and Tamás, M.J. (2010) How *Saccharomyces cerevisiae* copes with toxic metals and metalloids. *FEMS Microbiol Rev* **34:** 925–951.

Wysocki, R., Bobrowicz, P., and Ulaszewski, S. (1997) The *Saccharomyces cerevisiae* ACR3 gene encodes a putative membrane protein involved in arsenite transport. *J Biol Chem* **272:** 30061–30066.

Wysocki, R., Chery, C.C., Wawrzycka, D., Van Hulle, M., Cornelis, R., Thevelein, J.M., and Tamás, M.J. (2001) The glycerol channel Fps1p mediates the uptake of arsenite and antimonite in *Saccharomyces cerevisiae*. *Mol Microbiol* **40:** 1391–1401.

Wysocki, R., Clemens, S., Augustyniak, D., Golik, P., Maciaszczyk, E., Tamás, M.J., and Dziadkowiec, D. (2003) Metalloid tolerance based on phytochelatins is not functionally equivalent to the arsenite transporter Acr3p. *Biochem Biophys Res Commun* **304:** 293–300.

Wysocki, R., Fortier, P.K., Maciaszczyk, E., Thorsen, M., Leduc, A., Odhagen, A., *et al*. (2004) Transcriptional activation of metalloid tolerance genes in *Saccharomyces cerevisiae* requires the AP-1-like proteins Yap1p and Yap8p. *Mol Biol Cell* **15:** 2049–2060.

Supporting information

Additional supporting information may be found in the online version of this article at the publisher's web-site.

Mathematical modeling of arsenic transport, intracellular distribution and detoxification processes in yeast

Supporting Information

Authors: Soheil Rastgou Talemi[1], Therese Jacobson[2], Vijay Garla[3], Clara Navarrete[2], Annemarie Wagner[4], Markus J. Tamás[2*], Jörg Schaber[2*]

[1]Otto-von-Guericke-Universität Magdeburg Medizinische Fakultät Institut für Experimentelle Innere Medizin
Leipziger Str. 44, 39120 Magdeburg, Germany; [2]Department of Chemistry and Molecular Biology, University of Gothenburg, S-405 30 Gothenburg, Sweden; [3]Yale Center for Medical Informatics, Yale University, 300 George Street, Suite 501, New Haven, CT 06520-8009, USA.; [4]Department of Applied Physics, Chalmers University of Technology, SE-421 96 Gothenburg, Sweden.

[*] To whom correspondence should be addressed:
Jörg Schaber
Phone: +49 391 67 14453
Fax:+49 391 67 13312
Email: schaber@med.ovgu.de

Markus J Tamás
Phone: +46-31-786 2548
Fax: +46-31-786 3910
E-mail: markus.tamas@cmb.gu.se

Contents

Scaling Data

As^{III} influx-efflux data

To study the effect of GSH knockdown on As^{III} uptake and efflux, *S. cerevisiae* strains derived from YPH98 (Spector *et al.*, 2001) were used (wild type (Y252) and *gsh1Δ-PRO2-1*) and not from W303-1A as in the rest of the study. Assuming similar As^{III} dynamics, we rescaled the measured intracellular arsenite of the Y252 strain ($As^{III}_{gsh1\Delta\text{-}PRO2\text{-}1}$) by equating the maxima of the two different wild type measurements:

$$As^{III}_{gsh1\Delta-PRO2\_Scaled} = As^{III}_{gsh1\Delta-PRO2} \cdot \frac{As^{III}_{max-W303-1A}}{As^{III}_{max-Y252}}$$

Hog1 phosphorylation data

Hog1 phosphorylation data was extracted from Thorsen *et al*. (Thorsen *et al.*, 2006), Figure 3-B. We used the ImageJ software (1.44p version, National Institute of Mental Health, Bethesda, Maryland, USA) to quantify corresponding western blots. Hog1 phosphorylation levels were scaled to phosphorylated Hog1, 5 min after addition of 0.4M NaCl, assuming that this value is the maximum Hog1 phosphorylation level (Table S7).

Fps1 phosphorylation data

Fps1 phosphorylation data was derived from Thorsen *et al.* (Thorsen et al., 2006)(SI Table S7). We assumed that phosphorylated Fps1 levels are at basal level before As^{III} stress, two hours after washing the cells in As^{III} free medium, both for wild type and *hog1Δ* cells. All Fps1 phosphorylation data were scaled to the Fps1 phosphorylation value in wild type cells one hour after As^{III} addition, which was set to 100%.

Methods

Parameter Estimation

Model implementation and parameter estimation was done with COPASI (version: 4.8) (Hoops *et al.*, 2006). Model parameters were estimated using Evolutionary Programming. The weighted Sum of Squared Residuals (*wSSR*) was used as objective function.

$$wSSR = \sum_{i=1}^{m} w_i \sum_{j=1}^{n} (\hat{y}_{i,j} - y_{i,j})^2$$

with i=1,…,m as the number of experiments, and j=1,…,n as the data pointed for experiment i. w_i represents the respective weight of experiment i, set to the inverse of the average of the respective time series with a correction factor accommodating the different number of data points for some experiments. $\hat{y}_{i,j}$ is the simulated value for data point number j within experiment i and $y_{i,j}$ is the measured data point j within experiment i. As^{III} uptake and efflux data for the wild type, *ycf1Δ*, *hog1Δ*, *acr3Δ*, *acr3Δhog1Δ* and *acr3Δycf1Δ* strains were used for parameter estimation (Fig. 1). In addition, Fps1 phosphorylation data (from wild type and *hog1Δ* mutant) and

Hog1 phosphorylation data (from wild type) were used for parameter estimation (Fig. 3).

Model Selection

Model selection was done using Modelmage software (Schaber *et al.*, 2011). In order to select the most parsimonious mathematical model, which best approximates the data, we used the Akaike Information Criterion corrected for small sample sizes (AIC_c). AIC_c is an information theoretic approach for model selection, based on Kullback-Leibler (K-L) concept of information lost when using a model to approximate full truth. The full truth includes an infinite number of parameters, which determine the systems output (Burnham & Anderson, 2010). The AIC_c is described as follows:

$$AIC_c = 2k + n\left(ln\left(\frac{2\pi \cdot wSSR}{n}\right) + 1\right) + \frac{2k(k+1)}{n-k-1}$$

where *K*, *n* and *wSSR* represent number of parameters, number of data points and the weighted sum of squared residuals, respectively. Finally, models were ranked according to AIC_c, where the model with the minimum AIC_c score was ranked first. The K-L confidence set comprised of all models for which their likelihood relative to the estimated K-L best model likelihood, be ≈ 1/8 (Burnham & Anderson, 2010). In order to select and compare the best approximating model(s) we calculated the Akaike weights (*AICw*) (Burnham & Anderson, 2002)

$$AICw_i = \frac{e^{-\frac{1}{2}\Delta_i}}{\sum_{r=1}^{R} e^{-\frac{1}{2}\Delta_r}}$$

where $\Delta_i = AIC_i - AIC_{min}$, with AIC_i being the *AICc* for model *i*, *i*=1, …, *R* according to ranking and AIC_{min} the minimal *AICc*. The *AICw's* can be considered as the weight of evidence in favour of a model given as a number between 0 and 1, i.e. the higher the weight, the closer the model is to the hypothetical true model (Burnham & Anderson, 2002). We considered those models as best approximating that had an *AICw > 0.125*.

Sensitivity Analysis

We conducted a local sensitivity analysis using COPASI and analyzed scaled (normalized) sensitivity, where the scaled sensitivity $S_{i,j}$ of a certain output $o_i(p_j)$ (concentration of the molecular species of interest at the end of simulation run) with respect to a certain parameter p_j change Δp_j is calculated as:

$$S_{i,j} = \frac{p_j}{o_i} \cdot \frac{\partial o_i}{\partial p_j} \approx \frac{\frac{o_i(p_j+\Delta p_j) - o_i(p_j)}{o_i}}{\frac{\Delta p_j}{p_j}}$$

Where $\Delta p_j = 0.001 \cdot p_j$.

Identifiability Analysis

We conducted profile likelihood based identifiability analysis (Raue *et al.*, 2009) using Copasi software as explained in literature (Schaber, 2012).

Models Setup Summary

Four components were implemented differently leading to different candidate models. Each of these four components can adopt two possible setups. Thus, 16 different combinations were generated. The alternative model formulations are indicated by dashed components in Fig. 2. For a better overview we shortlist the components and their setups:

A) As^{III}-GSH conjugation

As^{III}-GSH conjugation was modeled in two different forms.

I. As^{III}_{in} directly converts to $As(GS)_3$.
II. As^{III}_{in} binds to $(GSH)_3$ and produces $As(GS)_3$, where initial $(GSH)_3$ concentration was assumed fixed and was estimated from experimental data.

B) *YCF1* gene expression

Two sets of models were designed based on different assumptions about cellular Ycf1 concentrations:

I. Ycf1 concentration was assumed fixed after preincubation in 0.1mM As^{III} containing medium.
II. Ycf1 concentration was higher in *acr3Δ* and *acr3Δhog1Δ* mutants (not *acr3Δycf1Δ* mutant) after preincubation with 0.1mM As^{III}.

C) vacuolar sequestration of $As(GS)_3$

Two kinetics were tested for vacuolar sequestration.

I. Mass action kinetics.
II. Michaelis-Menten kinetics.

D) As^{III} efflux through Acr3

Two kinetics were tested for As^{III} export through Acr3.

I. Mass action kinetics.
II. Michaelis-Menten kinetics.

Mathematical formulation of models is explained in Tables S2-S6. The order of mathematical details in these tables is explained below:

Table S2:
This table lists the algebraic and ordinary differential equations of the master model.

Table S3:
This table lists the rate laws for the reactions from Table S2 and details the differences between the model alternatives.

Table S4:
This table lists the state variables and their initial conditions. As models are initially set to steady state, some initial conditions could be derived from those that are estimated. The latter are listed in Table S6.

Table S5:
This table lists auxiliary variables and physical quantities including volume, Molar weight and cell surface calculation.

Table S6:
This table lists all estimated parameters including rate constants and initial conditions.

Theoretical Implementation of GSH Knockdown

In order to implement GSH knockdown in the model we used a knockdown factor, GSHknockdown-f. The GSH knockdown factor multiplies to initial GSH concentration in the set of models with GSH binding mechanisms. In the set of models which use direct conversion of As^{III} to $AsGS_3$, this factor multiplies in the rate law. The mathematical notation is explained in the supplementary Table S5. This factor is derived from (Spector et al., 2001). In this paper authors state that Δ*gsh1PRO2–1* cell extracts could support the growth of Δ*gsh1* cells with the efficiency similar to that of wild type extracts diluted 150-fold. Thus, they conclude that the GSH produced in GSH knockdown mutant is 0.5%-1.0% of that of wild type. As they didn't quantified the GSH content of the cells we quantified an autoradiogram in that paper (Fig.2.C), which is a more direct measure of cellular GSH content, both for Δgsh1PRO2–1 mutant and wild type cells. We quantified the autoradiogram and considered the 3 hour labeling intensity of Δ*gsh1* as background remove the background from 3 hour labeling intensity of wt and Δ*gsh1PRO2–1.* The ratio of 3 hour labeling intensity of Δ*gsh1PRO2–1* over 3 hour labeling intensity of wt considered as $GSH_{knockdown\text{-}f}$. The $GSH_{knockdown\text{-}f}$ is equal to 30% (0.3).

Modified Model Changes

A simple constant flux reaction is added to the best ranked model for GSH production and no GSH degradation is implemented.
$k_{GSH\text{-}production} = 0.02$ ($\mu mol \cdot lit^{-1} \cdot Sec^{-1}$)
The initial concentration of state variables were set as below (Concentrations are in $\mu mol \cdot lit^{-1}$ unit):

$[Acr3]_0 = 0.0004$
$[As^{III}_{in}]_0 = 10.1584$
$[As^{III}_{prot}]_0 = 142.7820$
$[As(GS)_3]_0 = 491.9193$
$[vAs(GS)_3]_0 = 154.5897$
$[Hog1]_0 = 0.1659$
$[Hog1PP]_0 = 0.0010$
$[Fps1]_0 = 0.0033$
$[Fps1P]_0 = 0.0266$
$[Ycf1]_0 = 0.0132$
$[GSH]_0 = 1600.0000$

Steady State Calculations

The steady state concentration of As^{III}_{in} and consequently As^{III}_{prot} are independent of $(GSH)_3$, Ycf1, $As(GS)_3$ and $vAs(GS)_3$ concentrations. If we consider more complex interactions the steady state concentration of As^{III}_{in} and consequently As^{III}_{prot} would be affected by the mode of regulation of the other As^{III} species. For example we included As^{III} induced GSH upregulation (Ycf1 is considered constant) and derived steady state concentration of As^{III}_{in} and other As^{III} species with respect to $vAs(GS)_3$.

$$(GSH)_{3-ss} = \sqrt{\frac{k_9 \cdot k_{15} \cdot k_{11} \cdot vAs(GS)_{3-ss}}{k_8 \cdot k_{16} \cdot k_{10} \cdot GSH_{knockdown-factor} \cdot Ycf1}}$$

$$As^{III}_{in-ss} = \sqrt{\frac{k_{16} \cdot k_9 \cdot k_{11} \cdot vAs(GS)_{3-ss}}{k_{15} \cdot k_8 \cdot k_{10} \cdot GSH_{knockdown-factor} \cdot Ycf1}}$$

$$As^{III}_{prot-ss} = \sqrt{\frac{(k_2)^2 \cdot k_{16} \cdot k_9 \cdot k_{11} \cdot vAs(GS)_{3-ss}}{(k_3)^2 \cdot k_{15} \cdot k_8 \cdot k_{10} \cdot GSH_{knockdown-factor} \cdot Ycf1}}$$

$$As(GS)_{3-ss} = \frac{GSH_{tot}}{\left(\frac{k_9}{k_8 \cdot As^{III}_{in-ss}} + \frac{k_{10} \cdot Ycf1}{k_{11}} + 1\right)}$$

$$V_{GSH-pro} = k_{15} \cdot As^{III}_{in} \cdot V_{cell-vac}$$

$$V_{GSH-deg} = k_{16} \cdot GSH \cdot V_{cell-vac}$$

k_{15} = As^{III} induced GSH rate constant

k_{16} = GSH degradation rate constant

Thus, in case we include As^{III} induced GSH upregulation (if enough experimental data available), As^{III} steady state concentration would be dependent on vacuolar sequestration of arsenite. Consequently, we can use it to more clearly investigate the efficiency of the vacuole in arsenite tolerance acquisition.

Sensitivity Analysis

In order to determine most important parameters governing As^{III} influx and efflux, and Fps1 phosphorylation we conducted local sensitivity analysis using best approximating model (SI: Methods).

Sensitivity analysis of the cellular arsenic at the end of 1.0 mM As^{III} exposure

The sensitivity analysis of the cellular As^{III} concentration up to the end of 1mM As^{III} exposure with respect to model kinetic parameters suggests that in wild type cells, the protein binding reaction rate constant (k_2) is the most sensitive parameter of the model, whereas in *acr3Δ* mutant, the GSH conjugation reaction rate constant (k_8) is the most sensitive one (Fig. S7).

Sensitivity analysis of the cellular arsenic after cell wash

Sensitivity analysis of the cellular As^{III} concentration after cell wash up to 2 hours with respect to model kinetic parameters for wild type cells, indicate that protein binding and dissociation rate constants (k_2 and k_3) are the most sensitive model parameters in terms of cellular As^{III} after cell wash, whereas in *acr3Δ* cells the As^{III}-GSH conjugation rate constant (k_8), is the most sensitive model parameter (Fig. S8).

Sensitivity analysis of Fps1 phosphorylation at the end of 1.0 mM As^{III} exposure

Sensitivity analysis of phosphorylated Fps1 concentration at the end of 1mM As^{III} exposure with respect to perturbation in model kinetic parameters suggest that

both in wild type and *acr3Δ* mutant, Fps1 dephosphorylation rate constant (k_7) and Hog1 dependent Fps1 phosphorylation rate constant (k_{6_Hog1}) are model's most sensitive parameters (Fig. S13).

Sensitivity analysis of the Fps1 phosphorylation after cell wash

Sensitivity analysis of the phosphorylated Fps1 concentration after cell wash up to 2 hours with respect to perturbation in model's kinetic parameters, suggest that Fps1 dephosphorylation rate constant (k_7) is the most sensitive model parameter both in wild type and *acr3Δ* mutant cells. Fps1 phosphorylation is much more sensitive to Hog1-dependent phosphorylation (k_{6_Hog1}) during As^{III} exposure than after cell wash. Also, Fps1 phosphorylation is more sensitive to perturbation in basal Fps1 phosphorylation rate constant (k_{6_basal}) after cell wash than As^{III} exposure (Fig. S14).

Identifiability Analysis

We conducted profile likelihood based identifiability analysis using Copasi software. 12 parameters out of 20 free parameters were practically identifiable. The Fps1 mediated As^{III} influx-efflux, protein binding and dissociation, Hog1 dephosphorylation, Basal Fps1 phosphorylation, Fps1 dephosphorylation, As^{III}_{in}-GSH conjugation and dissociation, vacuolar export of $vAs(GS)_3$, initial value of As^{III}_{in}, initial concentration of GSH in *acr3Δ* and *acr3Δhog1Δ* are practically identifiable (Fig. S2).

Supplementary Figures

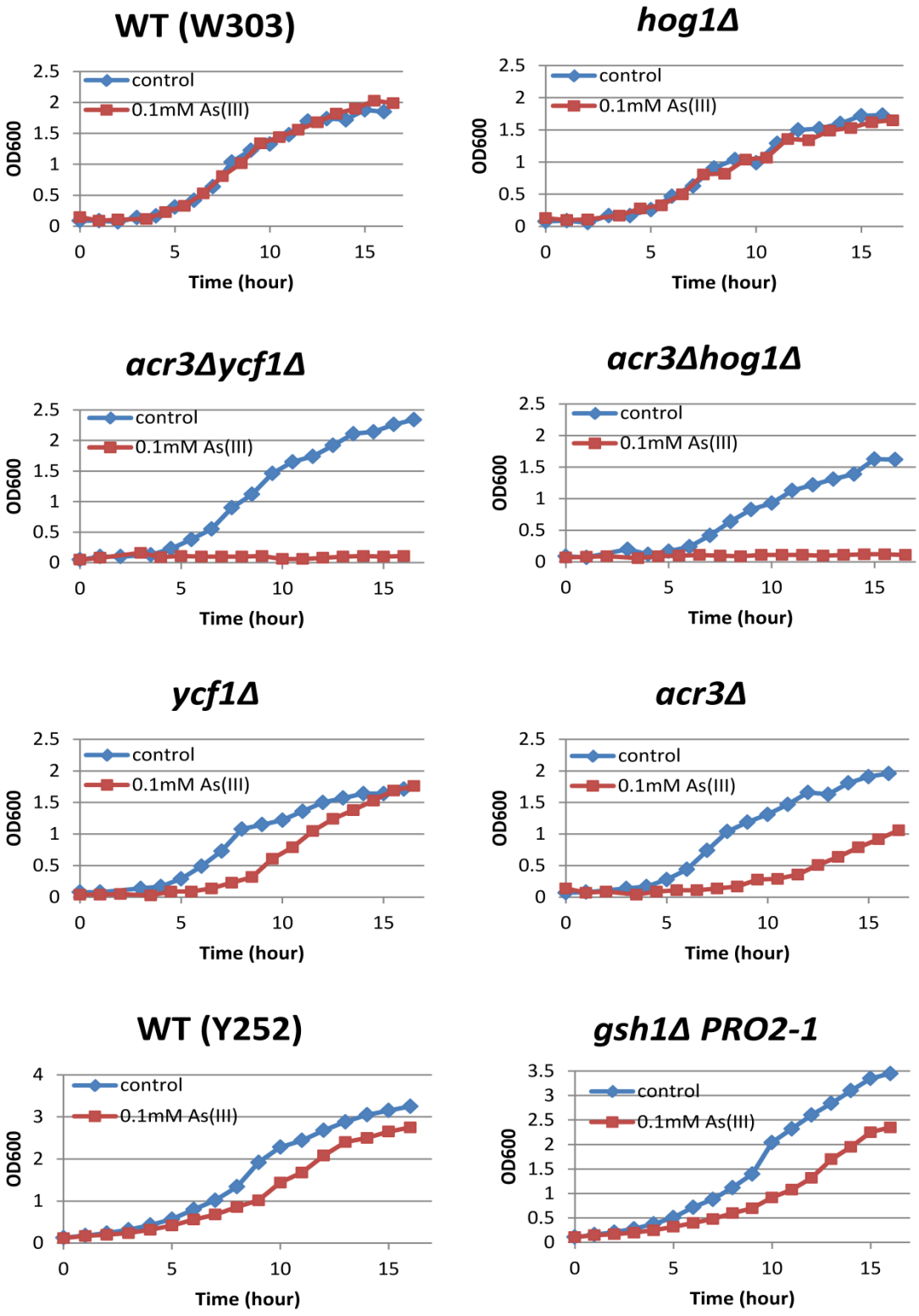

Supplementary Figure 1: Growth measurements of different strains under 0.1mM As^{III} stress. Growth of wild type and mutants in the absence (control) and presence of 0.1 mM As^{III} was monitored by measuring the optical density (OD) at 600 nm.

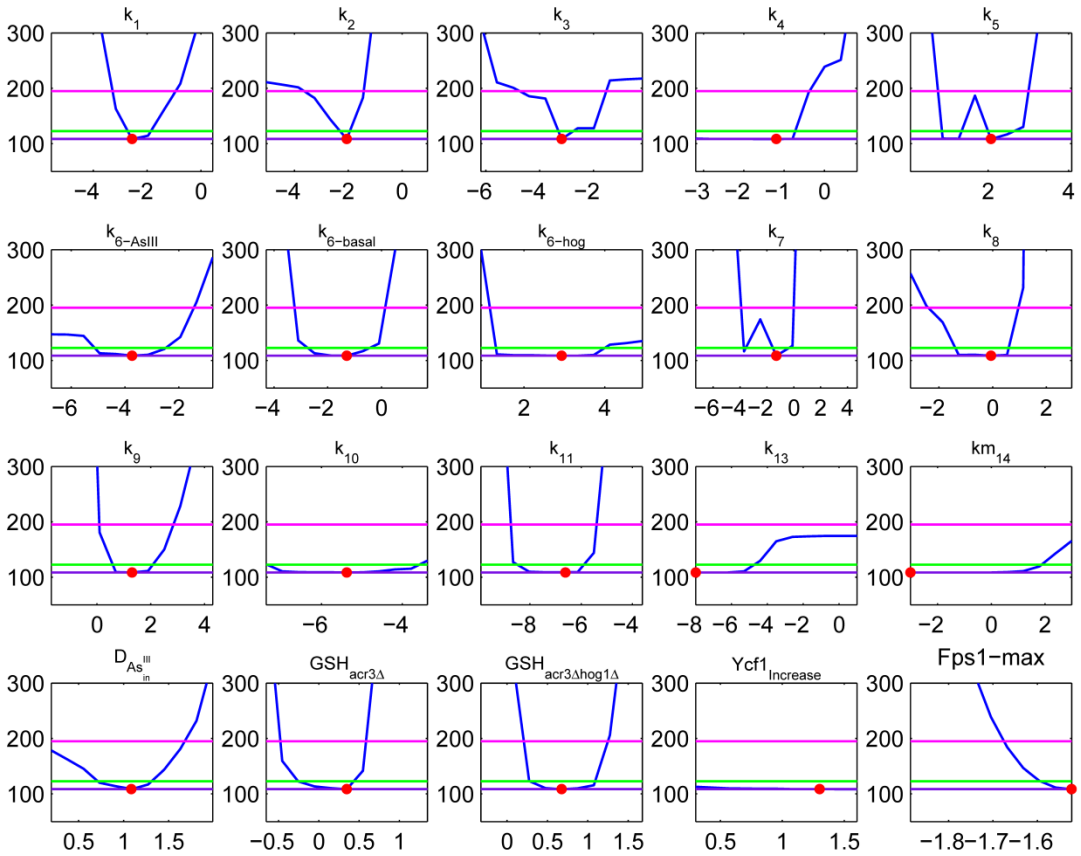

Supplementary Figure 2: Profile Likelihood based Identifiability analysis of model's free parameters. 95% confidence region is calculated by 2 methods, likelihood contours (pink line) and likelihood ratio (green line). The minimum objective value reached is shown at bottom (violet line) and the estimated parameter value is shown by a bold dot (•).Results show that 15 parameters out of 20 free parameters are practically identifiable based on likelihood ratio definition. In primary analysis vm_{14} was determined structurally non-identifiable.

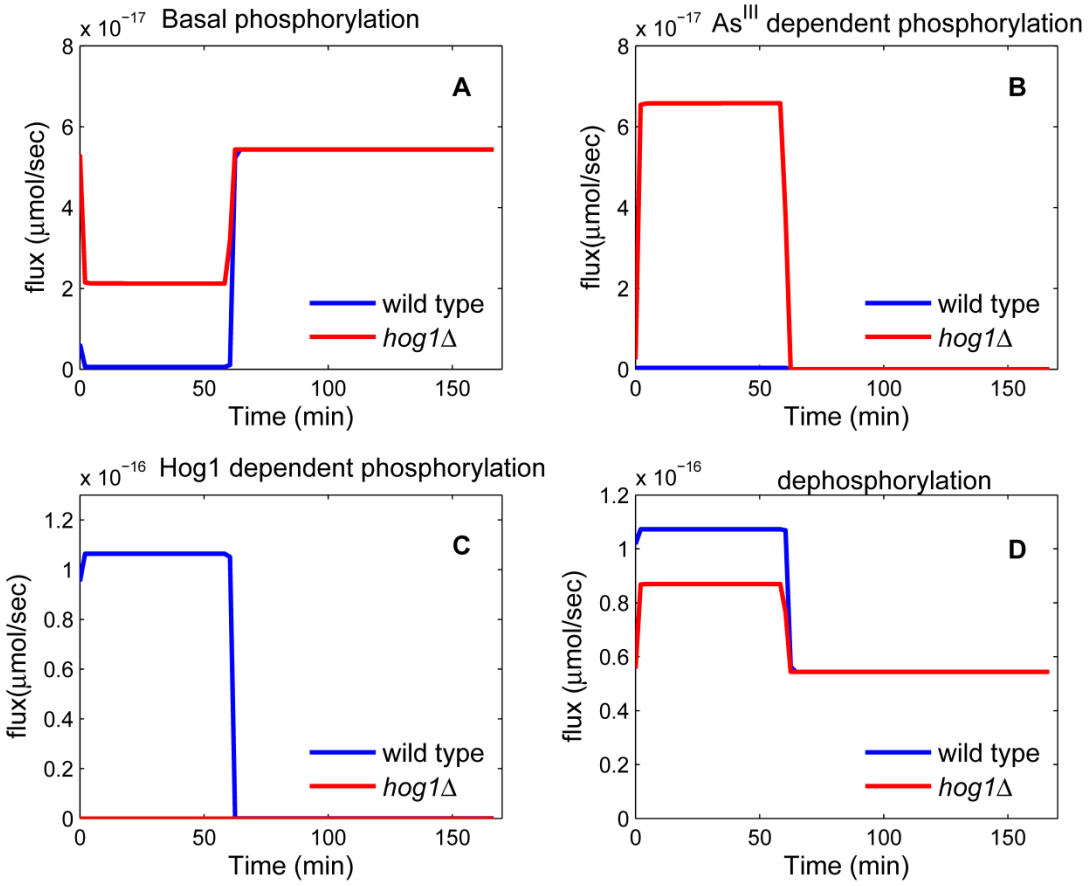

Supplementary Figure 3: Simulated Fps1 phosphorylation and dephosphorylation flux in wild type and *hog1Δ* mutant. Fps1 phosphorylation (v_{6_basal},v_{6_Hog1PP}, v_{6_AsIII}) and dephosphorylation fluxes (v_7) are simulated using the best ranked model. (**A**) Simulation of Fps1 phosphorylation flux by basal phosphorylation branch (v_{6_basal} in Figure 2). (**B**) Simulation of Fps1 phosphorylation flux by As^{III}_{in} dependent phosphorylation branch (v_{6_AsIII} in Figure 2). (**C**) Simulation of Fps1 phosphorylation flux by Hog1 dependent phosphorylation branch (v_{6_Hog1PP} in Figure 2). (**D**) Fps1 dephosphorylation flux (v_7 in Figure 2).

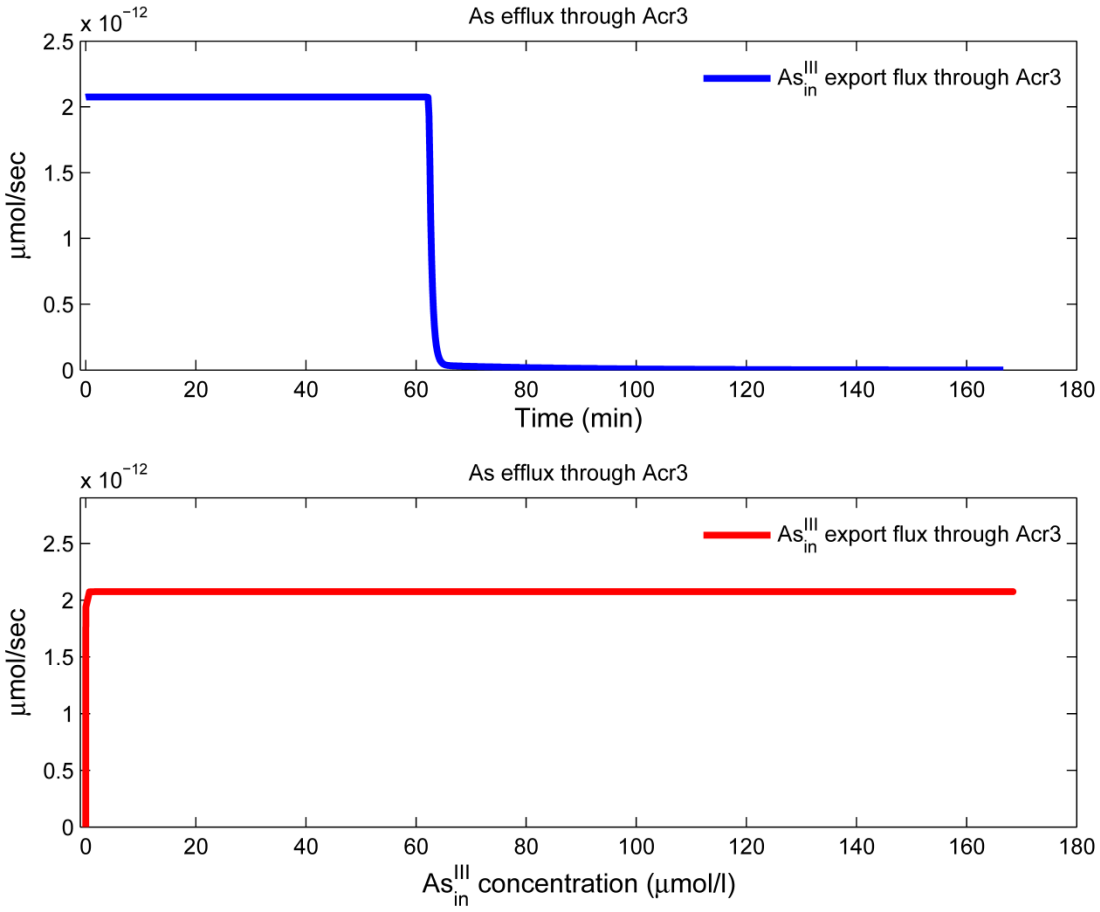

Supplementary Figure 4: As^{III} export flux through Acr3 (flux.v20).
As^{III}_{in} flux through Acr3 is simulated after 1mM As^{III} stress during exposure and 2 hours after cell wash. Simulation suggests rapid flux saturation over time (Top panel). This rapid saturation is because of Acr3 mediated As^{III} flux saturation in low As^{III}_{in} concentrations (Bottom panel).

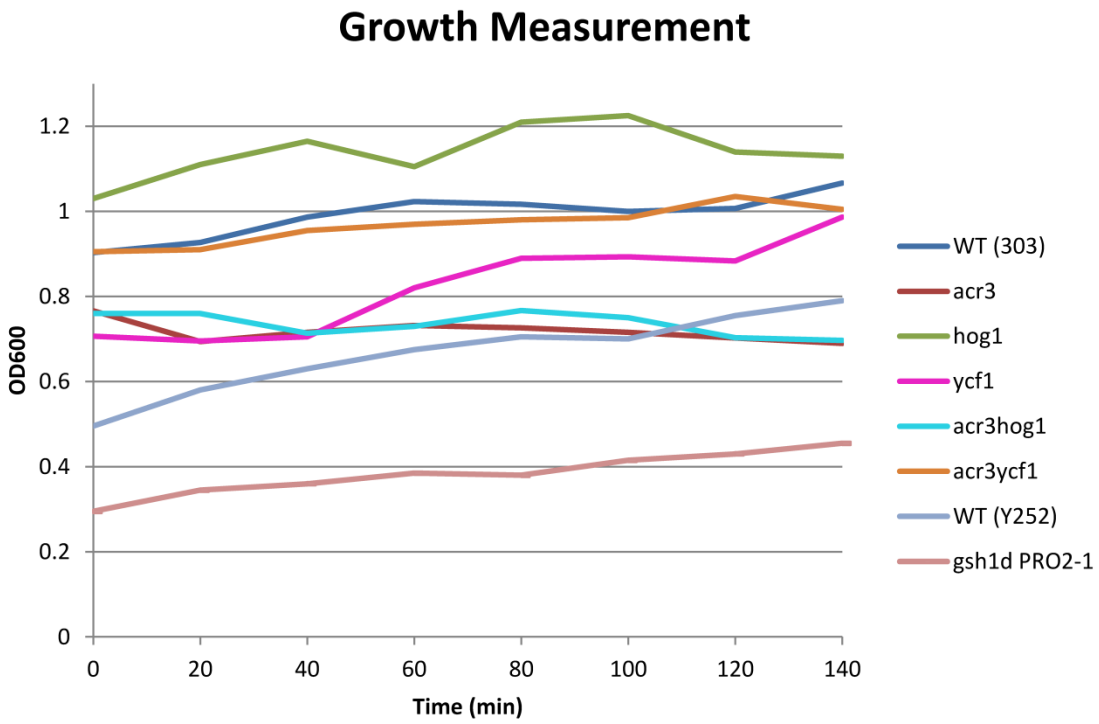

Supplementary Figure 5: Growth measurements during 1.0 mM As^{III} exposure and after cell wash. 1.0 mM As^{III} was added to cells at t=0 min. At t=60 min, the cells were washed to remove extracellular As^{III}. Growth was monitored by measuring the optical density (OD) at 600 nm.

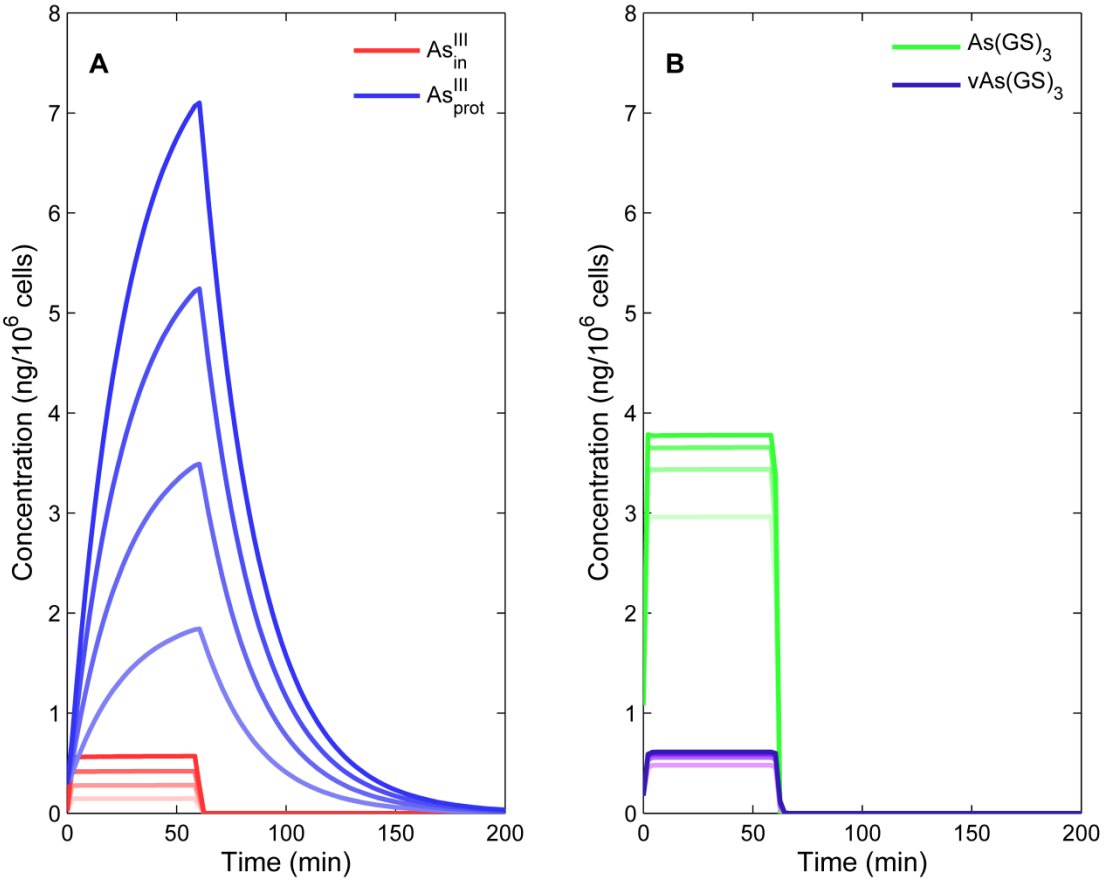

Supplementary Figure 6: Simulation of different arsenic species in response to increasing As^{III} concentrations. As^{III}_{ex} concentration increases from 0.5 to 2 mM (lighter colors and darker colors are output of lower and higher As^{III} stress, respectively). Simulation for wild type cells was done using best approximating model. (**A**) Simulation of As^{III}_{in} and As^{III}_{prot}. (**B**) Simulation of $As(GS)_3$ and $vAs(GS)_3$.

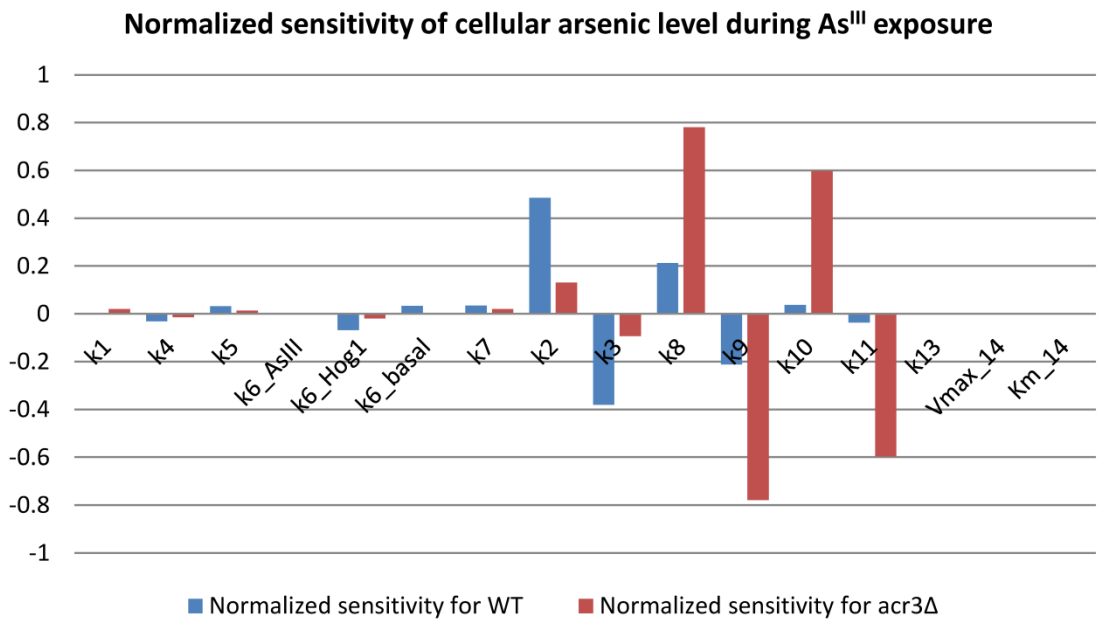

Supplementary Figure 7: Sensitivity analysis of total cellular arsenic level during As^{III} exposure.

Here we conducted the sensitivity analysis for total cellular arsenic level with respect to model kinetic parameters perturbation, both for wild type and *acr3Δ* mutant during As^{III} exposure. The plot represents normalized sensitivity versus different model parameters. The normalized sensitivity is the change in the output with respect to parameter perturbation which are normalized to their values before each calculation step (i,j). This is expressed in the mathematical formula in the supplementary information section “Sensitivity Analysis”. The ordinates are dimensionless quantities. The higher sensitivity of a parameter means the lower robustness of the considered output with respect to the corresponding parameter.

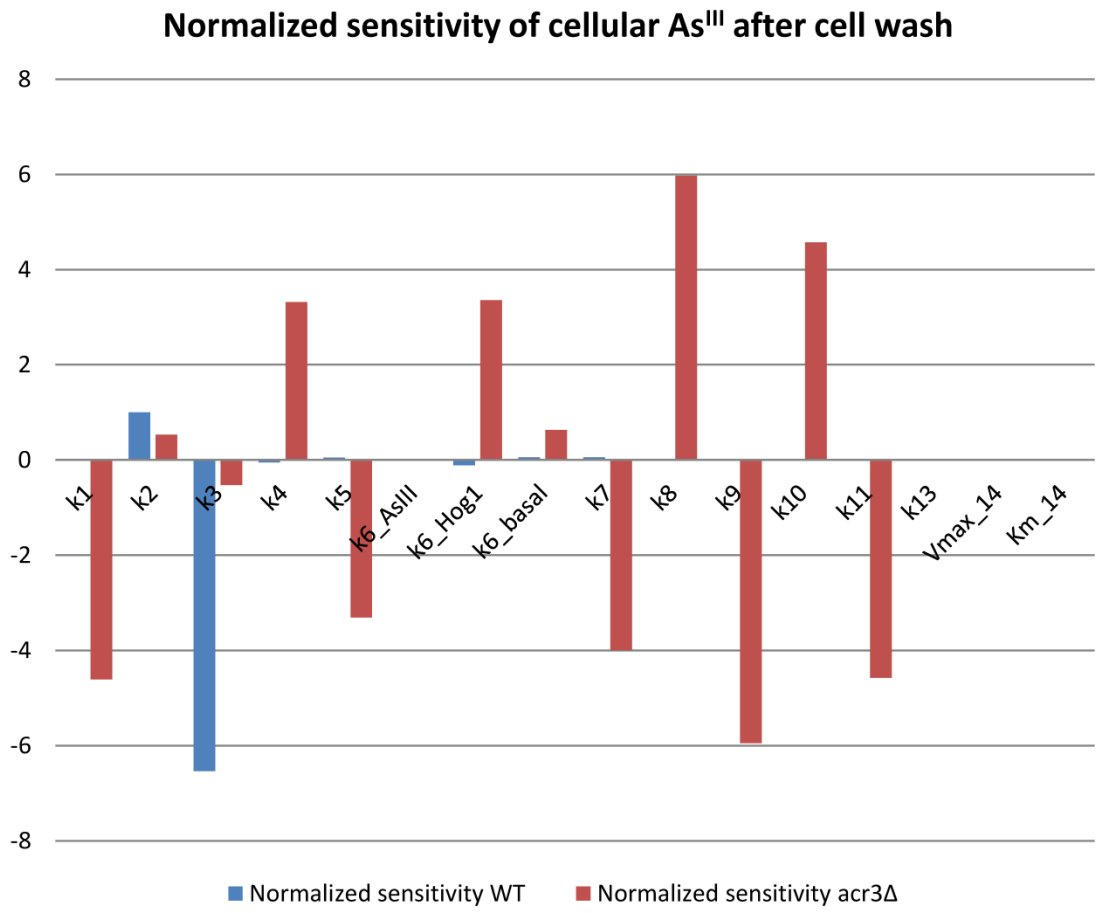

Supplementary Figure 8: Sensitivity analysis of total cellular arsenic level cell wash. Here we conducted the sensitivity analysis for total cellular arsenic level with respect to model kinetic parameters perturbation, both for wild type and *acr3Δ* mutant after cell wash. The plot represents normalized sensitivity versus different model parameters. The normalized sensitivity is the change in the output with respect to parameter perturbation which are normalized to their values before each calculation step (i,j). This is expressed in the mathematical formula in the supplementary information section "Sensitivity Analysis". The ordinates are dimensionless quantities. The higher sensitivity of a parameter means the lower robustness of the considered output with respect to the corresponding parameter.

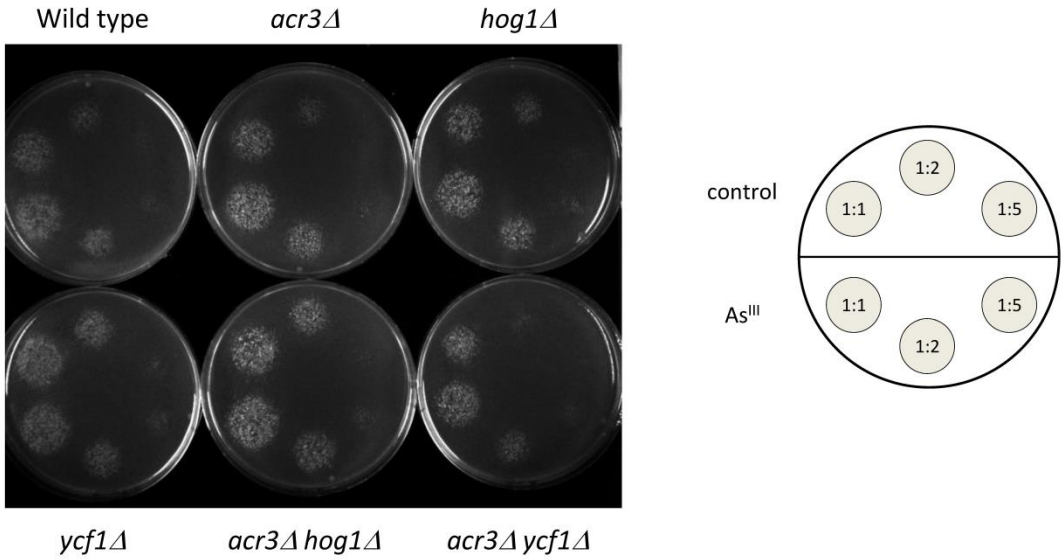

Supplementary Figure 9: Cells lacking ACR3 produce more GSH during As^{III} exposure than cells harboring a functional ACR3 gene. Cells lacking ACR3 produce more GSH during AsIII exposure than cells harboring a functional ACR3 gene. Cross-feeding assay. Precultures of the strains above were grown for about 19h and then split into two halves; one half was treated with 0.1 mM AsIII for 6h whereas the other half was left untreated (control). Thereafter, 10 OD units of cells were harvested, washed in 1ml ice-cold water and resuspended in 1 ml water. The cells were then broken by boiling, briefly centrifuged to remove cell debris and the supernatants collected. 5µl of each supernatant were spotted (undiluted 1:1, diluted 1:2, diluted 1:5) on top of a lawn of *gsh1Δ* cells (the *gsh1Δ* mutant cannot proliferate unless GSH is provided exogenously). After incubating the plates at 30°C for about 24h, a halo of proliferating *gsh1Δ* cells was visible around the spotted supernatants. The size of the halo is an indirect measure of the GSH present in the supernatants, and thus the GSH produced by untreated and As^{III} treated cells. For a more thorough description of the glutathione cross-feeding assay, see Thorsen et al, 2012 (Thorsen *et al.*, 2012).

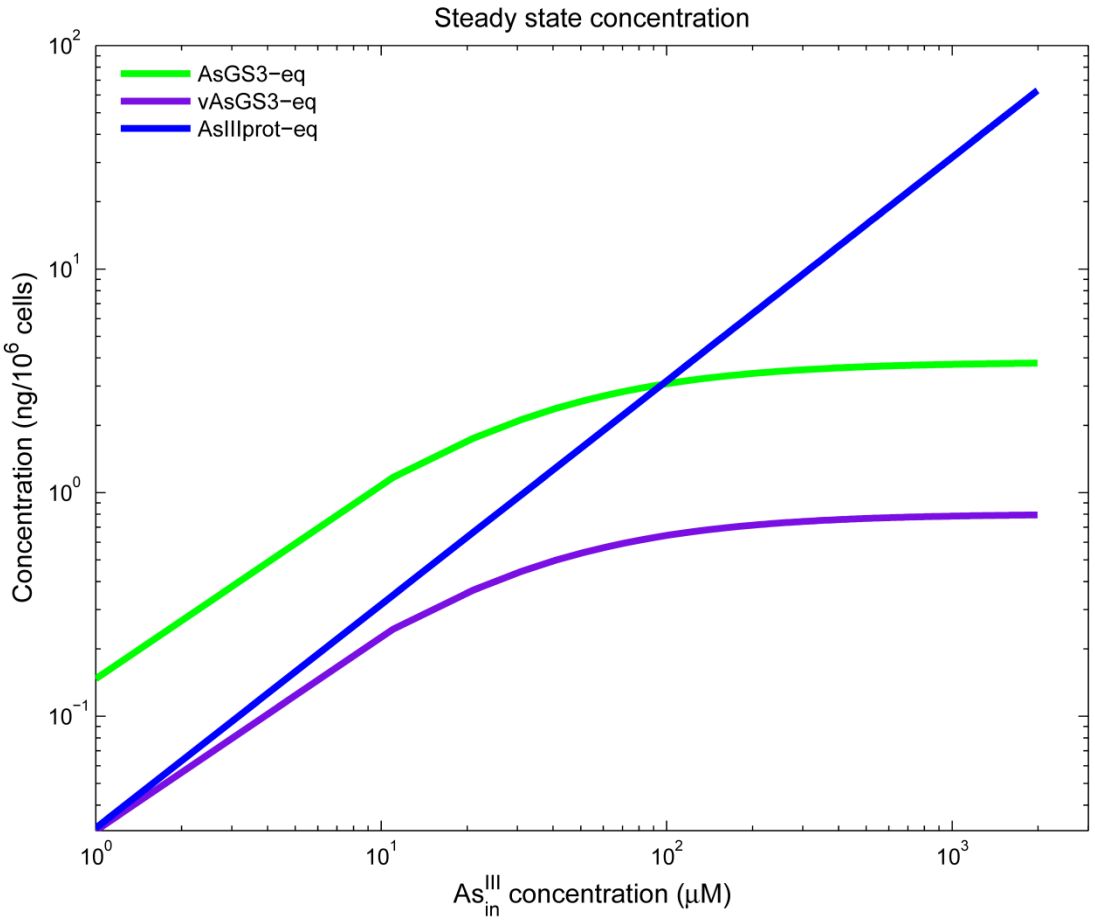

Supplementary Figure 10: Log-Log plot of arsenic species steady state concentration versus As^{III}_{in} concentration in wild type cells. Calculations suggest that As^{III}_{prot} concentration linearly increase with As^{III}_{in}, whereas $As(GS)_3$ and $vAs(GS)_3$ concentrations saturate gradually from 10 µM As^{III}_{in} concentration.

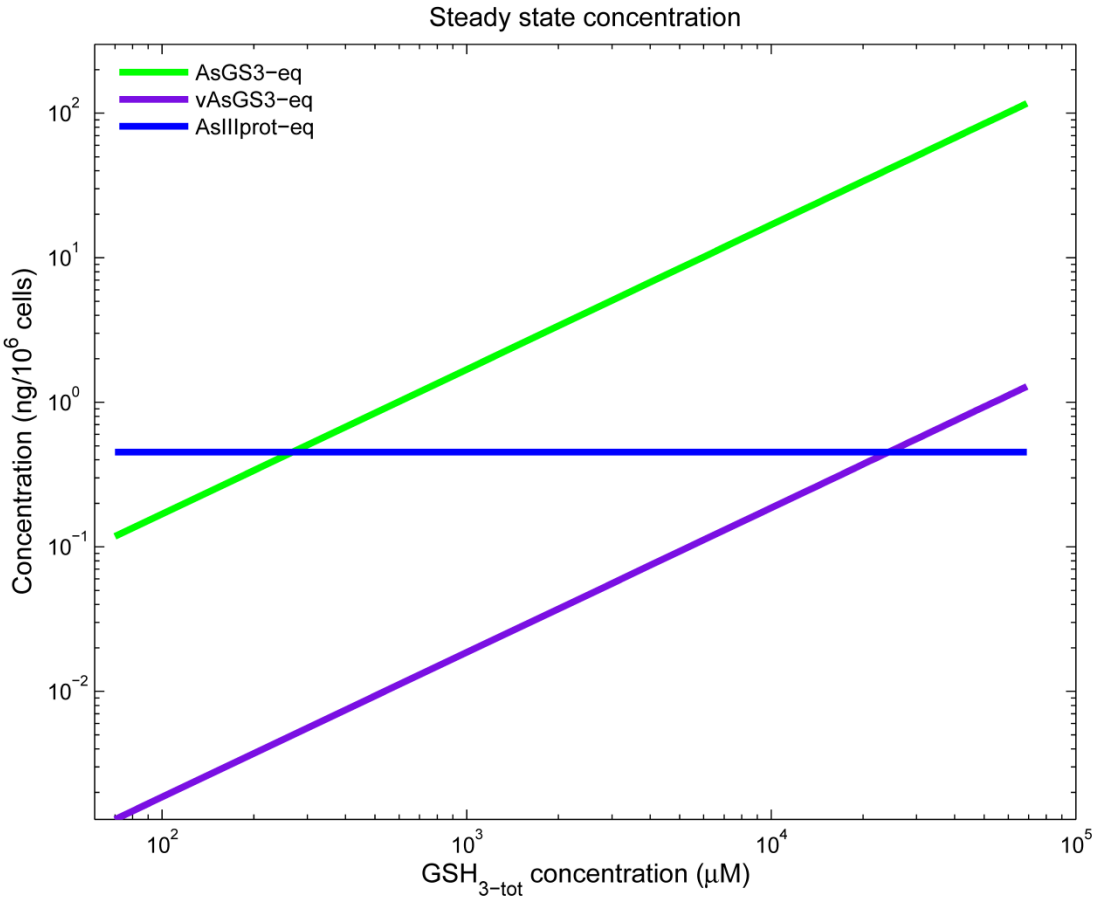

Supplementary Figure 11: Log-Log plot of arsenic species steady state concentration versus total GSH concentration in wild type cells. Calculations suggest that $As(GS)_3$ and $vAs(GS)_3$ concentrations significantly increase upon cellular GSH upregulation, whereas As^{III}_{prot} stays constant.

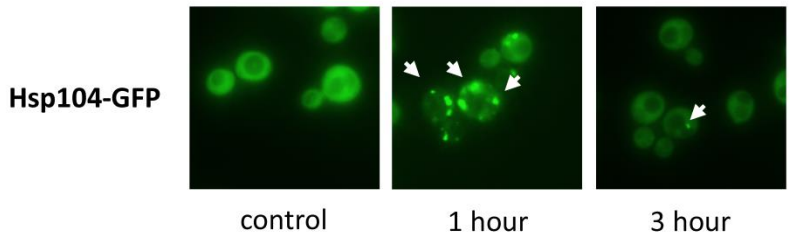

Supplementary Figure 12: As^{III} triggers protein aggregation/Hsp104 redistribution. Hsp104–GFP localization was monitored by fluorescence microscopy in living wild type cells before (control) and after addition of 0.5 mM As^{III} to the cell culture. Hsp104-GFP foci (indicated by arrows) represent sites of protein aggregation (Jacobson *et al.*, 2012)**.**

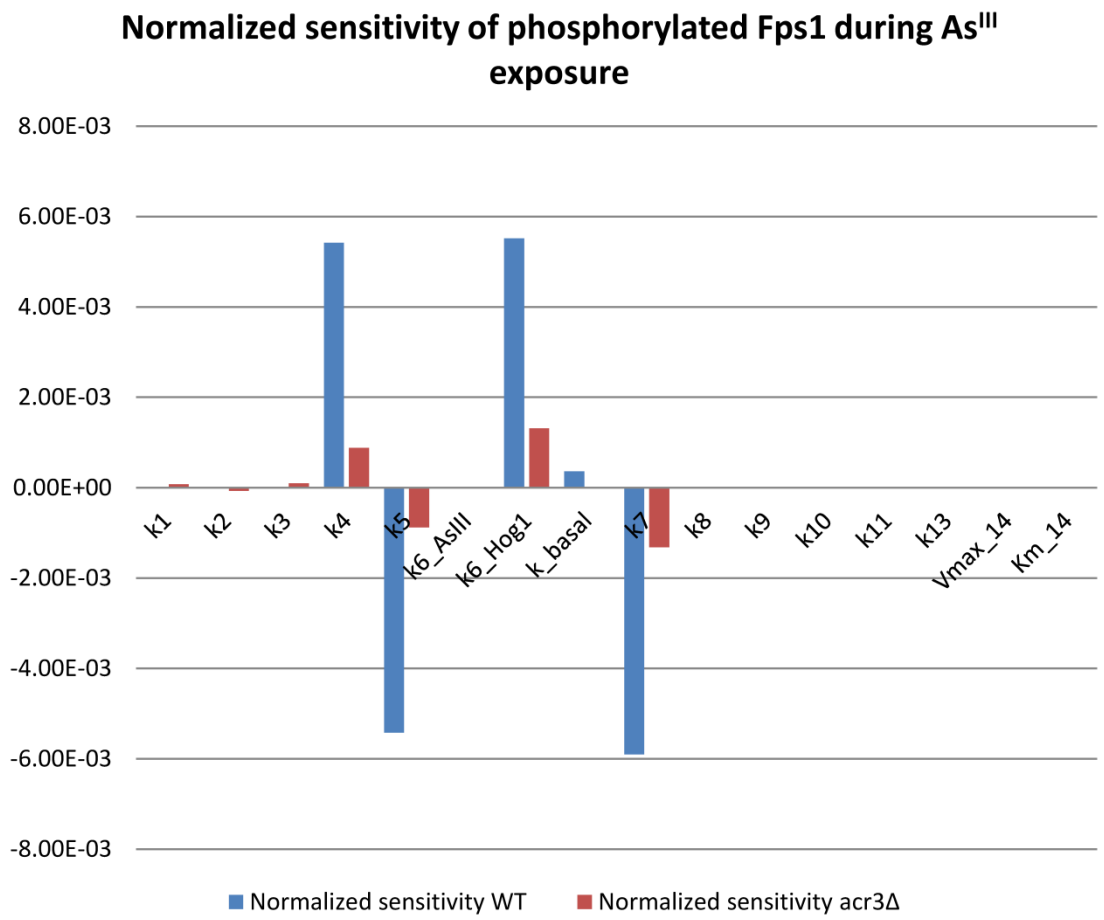

Supplementary Figure 13: Sensitivity analysis of cellular Fps1-p level during As^{III} exposure. Here we conducted the sensitivity analysis for cellular Fps1-p level with respect to model kinetic parameters perturbation, both for wild type and *acr3Δ* mutant during As^{III} exposure. The plot represents normalized sensitivity versus different model parameters. The normalized sensitivity is the change in the output with respect to parameter perturbation which are normalized to their values before each calculation step (i,j). This is expressed in the mathematical formula in the supplementary information section "Sensitivity Analysis". The ordinates are dimensionless quantities. The higher sensitivity of a parameter means the lower robustness of the considered output with respect to the corresponding parameter.

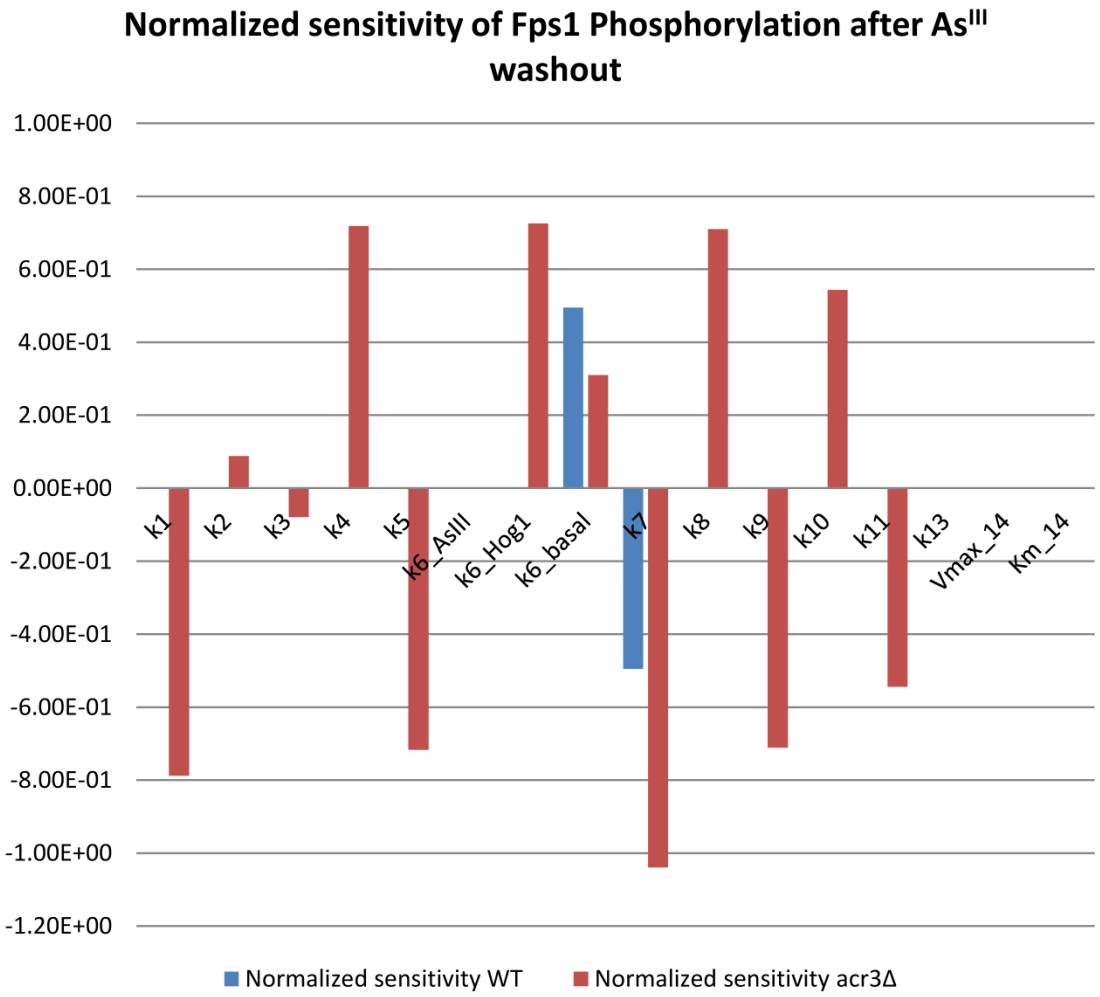

Supplementary Figure 14: Sensitivity analysis of cellular Fps1-p level after cell wash. Here we conducted the sensitivity analysis for cellular Fps1-p level with respect to model kinetic parameters perturbation, both for wild type and *acr3Δ* mutant after cell wash. The plot represents normalized sensitivity versus different model parameters. The normalized sensitivity is the change in the output with respect to parameter perturbation which are normalized to their values before each calculation step (i,j). This is expressed in the mathematical formula in the supplementary information section "Sensitivity Analysis". The ordinates are dimensionless quantities. The higher sensitivity of a parameter means the lower robustness of the considered output with respect to the corresponding parameter.

References

Burnham, K.P. & D.R. Anderson, (2002) *Model Selection and Multi-Model Inference: A Practical Information-theoretic Approach*, p. 496. Springer, New York.

Burnham, K.P. & D.R. Anderson, (2010) *Model Selection and Multi-Model Inference: A Practical Information-Theoretic Approach*, p. 60-20. Springer.

Hoops, S., S. Sahle, R. Gauges, C. Lee, J. Pahle, N. Simus, M. Singhal, L. Xu, P. Mendes & U. Kummer, (2006) COPASI--a COmplex PAthway SImulator. *Bioinformatics* **22**: 3067-3074.

Jacobson, T., C. Navarrete, S.K. Sharma, T.C. Sideri, S. Ibstedt, S. Priya, C.M. Grant, P. Christen, P. Goloubinoff & M.J. Tamas, (2012) Arsenite interferes with protein folding and triggers formation of protein aggregates in yeast. *J Cell Sci* **125**: 5073-5083.

Raue, A., C. Kreutz, T. Maiwald, J. Bachmann, M. Schilling, U. Klingmuller & J. Timmer, (2009) Structural and practical identifiability analysis of partially observed dynamical models by exploiting the profile likelihood. *Bioinformatics* **25**: 1923-1929.

Schaber, J., (2012) Easy parameter identifiability analysis with COPASI. *Biosystems*.

Schaber, J., M. Flottmann, J. Li, C.F. Tiger, S. Hohmann & E. Klipp, (2011) Automated ensemble modeling with modelMaGe: analyzing feedback mechanisms in the Sho1 branch of the HOG pathway. *PLoS One* **6**: e14791.

Spector, D., J. Labarre & M.B. Toledano, (2001) A genetic investigation of the essential role of glutathione: mutations in the proline biosynthesis pathway are the only suppressors of glutathione auxotrophy in yeast. *J Biol Chem* **276**: 7011-7016.

Thorsen, M., Y. Di, C. Tangemo, M. Morillas, D. Ahmadpour, C. Van der Does, A. Wagner, E. Johansson, J. Boman, F. Posas, R. Wysocki & M.J. Tamas, (2006) The MAPK Hog1p modulates Fps1p-dependent arsenite uptake and tolerance in yeast. *Mol Biol Cell* **17**: 4400-4410.

Thorsen, M., T. Jacobson, R. Vooijs, C. Navarrete, T. Bliek, H. Schat & M.J. Tamas, (2012) Glutathione serves an extracellular defence function to decrease arsenite accumulation and toxicity in yeast. *Mol Microbiol* **84**: 1177-1188.

Table S1: Yeast strains and plasmids used in this study

Name	Genotype/description	Source/reference
W303-1A	MAT**a** *ura3-1 leu2-3/112 trp1-1 his3-11/15 ade2-1 can1-100 GAL SUC2 mal0*	(Thomas & Rothstein, 1989)
RW118	W303-1A *ycf1*Δ::*loxP*	(Wysocki *et al.*, 2001)
RW104	W303-1A *acr3Δ::loxP-kanMX-loxP*	(Wysocki et al., 2001)
RW105	W303-1A *acr3Δ::loxP-kanMX-loxP ycf1Δ::loxP*	(Wysocki et al., 2001)
YSH444	W303-1A *hog1Δ::TRP1*	S. Hohmann
EDO1	W303-1A *acr3Δ::loxP-kanMX-loxP hog1Δ::TRP1*	(Thorsen *et al.*, 2006)
gsh1Δ	BY4741 (MATa;his3*Δ1; leu2Δ0; met15Δ0; ura3Δ0) gsh1Δ::KanMX4*	EUROSCARF
Y252	MAT**a** *ura3-52 lys2-801^{amber} ade2-101^{ochre} trp1-Δ1 leu2-Δ1*	(Spector *et al.*, 2001)
Y252 *gsh1Δ PRO2-1*	Y252 *gsh1Δ::LEU2 PRO2-1*	(Spector et al., 2001)
BY4741 *HSP104-GFP*	*MAT**a** his3Δ1 leu2Δ0 met15Δ0 ura3Δ0 HSP104-GFP-HIS3-MX6*	Invitrogen
BY4741 *HSP104-GFP gsh1Δ*	BY4741 *HSP104-GFP-HIS3-MX6 gsh1Δ::KanMX4*	This work
Plasmids		
SpPCS1	*S. pombe PCS1* gene under control of *GAL1* promoter in pYES2	(Clemens *et al.*, 1999)
pYES2	2μ, *GAL1* promoter, *URA3*	Invitrogen

Clemens, S., E.J. Kim, D. Neumann & J.I. Schroeder, (1999) Tolerance to toxic metals by a gene family of phytochelatin synthases from plants and yeast. *EMBO J* **18**: 3325-3333.

Spector, D., J. Labarre & M.B. Toledano, (2001) A genetic investigation of the essential role of glutathione: mutations in the proline biosynthesis pathway are the only suppressors of glutathione auxotrophy in yeast. *J Biol Chem* **276**: 7011-7016.

Thomas, B.J. & R. Rothstein, (1989) Elevated recombination rates in transcriptionally active DNA. *Cell* **56**: 619-630.

Thorsen, M., Y. Di, C. Tangemo, M. Morillas, D. Ahmadpour, C. Van der Does, A. Wagner, E. Johansson, J. Boman, F. Posas, R. Wysocki & M.J. Tamas, (2006) The MAPK Hog1p modulates Fps1p-dependent arsenite uptake and tolerance in yeast. *Mol Biol Cell* **17**: 4400-4410.

Wysocki, R., C.C. Chery, D. Wawrzycka, M. Van Hulle, R. Cornelis, J.M. Thevelein & M.J. Tamas, (2001) The glycerol channel Fps1p mediates the uptake of arsenite and antimonite in Saccharomyces cerevisiae. *Mol Microbiol* **40**: 1391-1401.

Table S2: Ordinary differential equation system of the master model.

Rates in {} indicate options. Volumes are in liter (l) and concentrations in (µmol/l).

ODE		
$As_{ex}^{III} = \begin{cases} [As_{ex}^{III}]_0 + \left([As_{ex}^{III}]_{shock} \cdot \left(1 - e^{\frac{As_{ex-t1}^{III} - Time}{As_{ex-tm}^{III}}} \right) \right) & \text{before washing out} \\ ([As_{ex}^{III}]_0 + [As_{ex}^{III}]_{shock}) \cdot e^{\frac{As_{ex-t2}^{III} - Time}{As_{ex-tm}^{III}}} & \text{after washing out} \end{cases}$		
As_{ex-t1}^{III}	0	Stress time (Seconds)
As_{ex-t2}^{III}	3600	Washing out time (seconds)

$$\frac{d([As_{in}^{III}] \cdot V_{cell-vac})}{dt} = -V_{cell-vac} \cdot \{v_{8-a}, v_{8-b}\} + V_{cell-vac} \cdot v_9 - V_{cell-vac} \cdot v_2 + V_{cell-vac} \cdot v_3 + Surface_{cell} \cdot v_1 - Surface_{cell} \cdot \{v_{14-a}, v_{14-b}\}$$

$$\frac{d([As_{prot}^{III}] \cdot V_{cell-vac})}{dt} = + V_{cell-vac} \cdot (v_2 - v_3)$$

$$\frac{d([Hog1PP] \cdot V_{cell})}{dt} = + V_{cell} \cdot (v_4 - v_5)$$

$$\frac{d([Hog1] \cdot V_{cell})}{dt} = + V_{cell} \cdot (-v_4 + v_5)$$

$$\frac{d([Fps1P] \cdot V_{cell})}{dt} = + V_{cell} \cdot (v_6 - v_7)$$

$$\frac{d([Fps1] \cdot V_{cell})}{dt} = + V_{cell} \cdot (-v_6 + v_7)$$

$$\frac{d([As(GS)_3] \cdot V_{cell-vac})}{dt} = -V_{cell-vac} \cdot v_9 + Surface_{vac} \cdot v_{11} + V_{cell-vac} \cdot \{v_{8-a}, v_{8-b}\} - Surface_{vac} \cdot \{v_{10-a}, v_{10-b}, v_{10-c}, v_{10-d}\}$$

$$\frac{d([vAs(GS)_3] \cdot V_{vac})}{dt} = -Surface_{vac} \cdot v_{11} + Surface_{vac} \cdot \{v_{10-a}, v_{10-b}, v_{10-c}, v_{10-d}\}$$

$$\frac{d([Acr3] \cdot V_{cell})}{dt} = + V_{cell} \cdot (v_{12} - v_{13})$$

$$\frac{d([(GSH)_3] \cdot V_{cell-vac})}{dt} = + V_{cell-vac} \cdot (v_9 - v_8)$$

Table S3: Rate equations of the master model including different model alternatives.

Concentrations are denoted by [] and initial concentration by $[]_0$. The auxiliary variables and parameters are described in Table S5. Volumes are in liter (l) and concentrations in (μmol/l).Bold parameters are free parameters that are estimated from data and their value is reported in Table S6.

Rate	Rate law	Description
v_1	$[\mathrm{Fps1}] \cdot \mathbf{k_1} \cdot \left([\mathrm{As^{III}_{ex}}] - [\mathrm{As^{III}_{in}}]\right)$	Arsenite influx-efflux reaction.
v_2	$\mathbf{k_2} \cdot [\mathrm{As^{III}_{in}}]$	Protein binding reaction.
v_3	$\mathbf{k_3} \cdot [\mathrm{As^{III}_{prot}}]$	Protein bound arsenite dissociation.
v_4	$\mathbf{k_4} \cdot k_{o-4} \cdot [\mathrm{As^{III}_{in}}] \cdot [\mathrm{Hog1}]$	Arsenic induced Hog1 phosphorylation.
v_5	$\mathbf{k_5} \cdot [\mathrm{Hog1PP}]$	Hog1PP dephosphorylation.
v_6	$[\mathrm{Fps1}] \cdot \left(\mathbf{k_{6-As^{III}}} + \mathbf{k_{6-Hog1PP}} \cdot [\mathrm{Hog1PP}] + \mathbf{k_{6-basal}}\right)$	Fps1 phosphorylation reactions.
v_7	$\mathbf{k_7} \cdot [\mathrm{Fps1P}]$	Fps1-P dephosphorylation.
$v_{8\text{-}a}$	$k_{o-8} \cdot \mathbf{k_8} \cdot \mathrm{GSH_{knockdown-f}} \cdot [\mathrm{As^{III}_{in}}] \cdot [\mathrm{GSH_3}]$	As^{III}-glutathione conjugation. $(GSH)_3$ binding is considered.
$v_{8\text{-}b}$	$k_{o-8} \cdot \mathbf{k_8} \cdot \mathrm{GSH_{knockdown-f}} \cdot [\mathrm{As^{III}_{in}}]$	As^{III}-glutathione conjugation. Direct As^{III} to $As(GS)_3$ conversion.
v_9	$\mathbf{k_9} \cdot [\mathrm{As(GS)_3}]$	$As(GS)_3$ dissociation.
$v_{10\text{-}a}$	$\frac{k_{o-10} \cdot [\mathrm{Ycf1}] \cdot \mathbf{V_{max10}} \cdot [\mathrm{As(GS)_3}]}{\mathbf{k_{m10}} + [\mathrm{As(GS)_3}]}$	Vacuolar sequestration of $As(GS)_3$.(first setup)
$v_{10\text{-}b}$	$\frac{k_{o-10} \cdot \mathbf{V_{max10}} \cdot [\mathrm{As(GS)_3}]}{\mathbf{k_{m10}} + [\mathrm{As(GS)_3}]}$	Vacuolar sequestration of $As(GS)_3$.(Second setup)
$v_{10\text{-}c}$	$k_{o-10} \cdot [\mathrm{Ycf1}] \cdot \mathbf{k_{10}} \cdot [\mathrm{As(GS)_3}]$	Vacuolar sequestration of $As(GS)_3$.(Third setup)
$v_{10\text{-}d}$	$k_{o-10} \cdot \mathbf{k_{10}} \cdot [\mathrm{As(GS)_3}]$	Vacuolar sequestration of $As(GS)_3$.(Fourth setup)
v_{11}	$\mathbf{k_{11}} \cdot [\mathrm{vAs(GS)_3}]$	$vAs(GS)_3$ export out of vacuole.
v_{12}	$k_{o-12} \cdot \mathbf{k_{12}} \cdot [\mathrm{As^{III}_{in}}]$	Acr3 protein translation.
v_{13}	$\mathbf{k_{13}} \cdot [\mathrm{Acr3}]$	Acr3 protein degradation.
$v_{14\text{-}a}$	$\frac{[\mathrm{Acr3}] \cdot \mathbf{V_{max14}} \cdot [\mathrm{As^{III}_{in}}]}{\mathbf{k_{m14}} + [\mathrm{As^{III}_{in}}]}$	As^{III} export through Acr3. (First setup)
$v_{14\text{-}b}$	$[\mathrm{Acr3}] \cdot \mathbf{k_{14}} \cdot [\mathrm{As^{III}_{in}}]$	As^{III} export through Acr3. (Second setup)

Table S4: State variables and their initial conditions.

Model's state variables and their initial concentrations are listed below. $[]_0$ indicates initial concentrations and concentrations are in (µmol/l). Bold parameters are free parameters that are estimated from data and their value is reported in Table S6.

State variable (Compartment)	Initial Concentration	Remark
Acr3 (Cell)	$\begin{cases} \frac{[\mathrm{Fps1}]_0 \cdot ([\mathrm{As}^{\mathrm{III}}_{\mathrm{ex}}]_0 - [\mathrm{As}^{\mathrm{III}}_{\mathrm{in}}]_0) \cdot (\mathbf{k_{m14}} + [\mathrm{As}^{\mathrm{III}}_{\mathrm{in}}]_0)}{\mathbf{v_{max14}} \cdot [\mathrm{As}^{\mathrm{III}}_{\mathrm{in}}]_0} & v_{14-a} \text{ is selected} \quad \mathrm{ACR3^+} \text{ mutants} \\ \frac{[\mathrm{Fps1}]_0 \cdot ([\mathrm{As}^{\mathrm{III}}_{\mathrm{ex}}]_0 - [\mathrm{As}^{\mathrm{III}}_{\mathrm{in}}]_0)}{\mathbf{k_{20}} \cdot [\mathrm{As}^{\mathrm{III}}_{\mathrm{in}}]_0} & v_{14-b} \text{ is selected} \\ 0 & \text{acr3Δ mutants} \end{cases}$	Acr3 concentration in the cell. Initial concentration was calculated according to steady state assumption.
Fps1 (Cell)	$\frac{0.03}{\frac{\mathbf{k_{6-As^{III}}} \cdot [\mathrm{As}^{\mathrm{III}}_{\mathrm{in}}]_0 + \mathbf{k_{6-Hog1PP}} \cdot [\mathrm{Hog1PP}]_0 + \mathbf{k_{6-basal}}}{\mathbf{k_7}} + 1}$	Total Fps1 concentration (Fps1 + Fps1P) was assumed fix and the corresponding value was extracted from http://yeastgfp.yeastgenome.org/ which is 0.03 (µmol/l) . Fps1 concentration is calculated according to steady state concentration.
Fps1P (Cell)	$\frac{\mathbf{k_{6-As^{III}}} \cdot [\mathrm{As}^{\mathrm{III}}_{\mathrm{in}}]_0 + \mathbf{k_{6-Hog1PP}} \cdot [\mathrm{Hog1PP}]_0 + \mathbf{k_{6-basal}}}{\mathbf{k_7}}$	Phosphorylated Fps1 (Fps1-P) concentration is calculated according to steady state assumption.
Hog1 (Cell)	$\begin{cases} \frac{0.167}{\frac{[\mathrm{As}^{\mathrm{III}}_{\mathrm{in}}]_0 \cdot \mathbf{k_4}}{\mathbf{k_5}} + 1} & \mathrm{HOG1^+} \text{mutants and wild type} \\ 0.167 & \text{hog1Δ mutants} \end{cases}$	Total Hog1 concentration (Hog1 + Hog1PP) is extracted from http://yeastgfp.yeastgenome.org/ which is 0.167 (µmol/lit) . Initial concentration of Hog1 is calculated according to steady state assumption.
Hog1PP (Cell)	$\begin{cases} \frac{[\mathrm{Hog1}]_0 \cdot [\mathrm{As}^{\mathrm{III}}_{\mathrm{in}}]_0 \cdot \mathbf{k_4}}{\mathbf{k_5}} & \mathrm{HOG1^+} \text{mutants and wild type} \\ 0 & \text{hog1Δ mutants} \end{cases}$	Hog1PP initial concentration is calculated according to steady state assumption.
Ycf1 (Cell)	$\begin{cases} 0.013151 & \text{not Ycf1 upregulation} \\ 0.013151 & \text{Ycf1 upregulation on models (ACR}^+ \text{ mutants and wild type)} \\ 0.013151 \cdot \Delta[\mathbf{Ycf1}] & \text{Ycf1 upregulation on models (acr3Δ mutants)} \end{cases}$	Initial concentration of Ycf1 is supposed to be the same for all strains containing *ACR3* (WT, *ycf1Δ*, *hog1Δ* and GSH knockdown) and is derived from http://yeastgfp.yeastgenome.org/. For acr3Δ mutants (except *acr3Δycf1Δ*), it is increased by Δ[Ycf1] factor which is estimated.
As^{III}_{in} (Cell-Vac)	$\begin{cases} \mathrm{As}^{\mathrm{III}}_{\mathrm{ex}-0} & \text{acr3Δ mutants} \\ \mathbf{As^{III}_{in-ACR3^+}} & \mathrm{ACR3^+} \text{ mutants and wild type} \end{cases}$	Initial arsenite concentration in $V_{cell-vac}$. This is estimated for wild type and is assumed to equal *acr3Δ* mutants.

$As(GS)_3$ (Cell-Vac)	$\begin{cases} \frac{\mathbf{k_8} \cdot GSH_{knockdown-factor} \cdot [As^{III}_{in}]_0 \cdot [(GSH)_3]_0}{k_9} & v_{8-a} \text{ is selected} \\ \frac{\mathbf{k_8} \cdot GSH_{knockdown-factor} \cdot [As^{III}_{in}]_0}{k_9} & v_{8-b} \text{ is selected} \end{cases}$	Glutathione conjugated arsenite $[As(GS)3]_0$ initial concentration is calculated according to steady state assumption.
$vAs(GS)_3$ (Vac)	$\begin{cases} \frac{\mathbf{v_{max10}} \cdot [Ycf1]_0 \cdot [As(GS)_3]_0}{\mathbf{k_{11}} \cdot (\mathbf{k_{m10}} + [As(GS)_3]_0)} & v_{10-a} \text{ is selected} \\ \frac{\mathbf{v_{max10}} \cdot [As(GS)_3]_0}{\mathbf{k_{11}} \cdot (\mathbf{k_{m10}} + [As(GS)_3]_0)} & v_{10-b} \text{ is selected} \\ \frac{\mathbf{k_{10}} \cdot [Ycf1]_0 \cdot [As(GS)_3]_0}{\mathbf{k_{11}}} & v_{10-c} \text{ is selected} \\ \frac{\mathbf{k_{10}} \cdot [As(GS)_3]_0}{\mathbf{k_{11}}} & v_{10-d} \text{ is selected} \\ 0 & ycf1\Delta \text{ is selected} \end{cases}$	Vacuole-sequestered arsenite. Initial concentration is calculated according to steady state assumption.
As^{III}_{prot} (Cell-Vac)	$\frac{\mathbf{k_2} \cdot [As^{III}_{in}]_0}{\mathbf{k_3}}$	Initial concentration of protein-bound arsenite is calculated using steady state assumption.
$(GSH)_3$ (Cell-Vac)	$\begin{cases} [(\mathbf{GSH})_3]_{\mathbf{0-acr3\Delta hog1\Delta}} & acr3\Delta hog1\Delta \\ [(\mathbf{GSH})_3]_{\mathbf{0-acr3\Delta}} & acr3\Delta \\ [(GSH)_3]_{0-ACR3^+} & ACR3^+ \text{ mutants and wild type} \end{cases}$	Glutathione initial concentration. $[(GSH)_3]_{0\text{-}ACR3^+}$ is explained in Table S5.
As^{III}_{ex} (medium)	100	As^{III}_{ex} concentration in medium (Table S2).

Table S5: A**uxiliary variables, physical quantities and their Definition/value.**

Concentrations are denoted by [] and $[]_0$ denotes the initial concentration. Bold parameters are free parameters that are estimated from data and their value is reported in Table S6. Volumes are in Liter, concentrations are in μmol/l.

Variable/Parameter	Definition/Value	Remark
k_{o-4}	$\begin{cases} 1 & HOG1^+ \text{ mutants and wild type} \\ 0 & hog1\Delta \text{ mutants} \end{cases}$	Acting as a switch which removes Hog1 phosphorylation reaction.
k_{o-8}	$\begin{cases} 1 & GSH^+ \text{ mutants and wild type} \\ 0 & \text{GSH knockdown mutants} \end{cases}$	Acting as a switch which is being used in GSH_damping_factor in GSH knockdown mutant (*gsh1Δ PRO2-1*).
k_{o-10}	$\begin{cases} 1 & YCF1^+ \text{ mutants and wild type} \\ 0 & ycf1\Delta \text{ mutants} \end{cases}$	Acting as a switch which cancels vacuolar sequestration.
k_{o-14}	$\begin{cases} 1 & ACR3^+ \text{ mutants and wild type} \\ 0 & acr3\Delta \text{ mutants} \end{cases}$	Acting as a switch which cancels Acr3 mediated As^{III} export.
$Asngpermil_{tot}$	$(As(GS)_3 + As_{in}^{III} + As_{prot}^{III}) \cdot AsMw \cdot V_{cell-vac} \cdot 10^9 + vAs(GS)_3 \cdot AsMw \cdot V_{vac} \cdot 10^9$	Total amount of arsenic (nanogram/10^6cells) which is being fitted to experimental data.
Fps1Pfit	$\frac{100 \cdot [Fps1P]}{\mathbf{Fps1P_{max}}}$	A variable which is used to fit Fps1 phosphorylation data. Because phosphorylated Fps1 data is relative.
Hog1PPfit	$\frac{100 \cdot [Hog1PP]}{Hog1_{sum}}$	A variable which is used to fit Hog1 phosphorylation data. Because phosphorylated Hog1 data is relative.
$Hog1_{sum}$	$[Hog1] + [Hog1PP]$	Total Hog1 concentration (Hog1 + Hog1PP) is extracted from http://yeastgfp.yeastgenome.org which is 0.167 (μmol/lit) . Initial concentration of Hog1 is calculated according to steady state assumption. Two different species of Hog1 are considered in these models.
$GSH_{knockdown-f}$	$\begin{cases} 0.2175 & \text{GSH knockdown } (k_{o-8} = 0) \\ 1 & GSH^+ \text{mutants and wild type } (k_{o-8} = 1) \end{cases}$	A coefficient which impose the knockdown effect in the model for *gsh1Δ PRO2-1* strain (Supplementary

		information, Theoretical implementation of GSH knockdown).
$[(GSH)_3]_{0\text{-}acr3\Delta hog1\Delta}$	$[(GSH)_3]_{0\text{-}ACR3^+} \cdot \mathbf{[(GSH)_3]_{r\text{-}acr3\Delta hog1\Delta}}$	Initial glutathione concentration in *acr3Δhog1Δ* mutant.
$[(GSH)_3]_{0\text{-}acr3\Delta}$	$[(GSH)_3]_{0\text{-}ACR3^+} \cdot \mathbf{[(GSH)_3]_{r\text{-}acr3\Delta}}$	Initial glutathione concentration in *acr3Δ* and *acr3Δycf1Δ* mutants.
$[(GSH)_3]_{0\text{-}ACR3^+}$	435.424	Initial glutathione concentration in $ACR3^+$ knockout mutants and wild type is considered three times reported value in Perrone et al. (Perrone *et al.*, 2005), as cells were pre-incubated for 24 hours in 0.1 mM As^{III} containing medium.
V_{cell}	$5 \cdot 10^{-14}$	*Saccharomyces cerevisiae* volume measured in glucose medium 1% (Vindelov & Arneborg, 2002).
V_{vac}	$2 \cdot 10^{-14}$	*Saccharomyces cerevisiae* vacuole volume approximated as 1/5 of cell volume (Vindelov & Arneborg, 2002).
$V_{cell\text{-}vac}$	$3 \cdot 10^{-14}$	*Saccharomyces cerevisiae* volume without vacuole volume.
V_{medium}	5·e-11	1000 times cell volume (Schaber *et al.*, 2010).
AsMw	74.9216	Arsenite molar weight (grams).
Surface_cell	$(36 \cdot \prod)^{1/3} \cdot V_{cell}^{2/3}$	Cell surface approximation. Cell is considered as a sphere.
Surface_vac	$(36 \cdot \prod)^{1/3} \cdot V_{vac}^{2/3}$	Vacuole surface approximation. Vacuole is considered as a sphere.

References:

Perrone, G.G., C.M. Grant & I.W. Dawes, (2005) Genetic and environmental factors influencing glutathione homeostasis in Saccharomyces cerevisiae. *Mol Biol Cell* **16**: 218-230.

Schaber, J., M.A. Adrover, E. Eriksson, S. Pelet, E. Petelenz-Kurdziel, D. Klein, F. Posas, M. Goksor, M. Peter, S. Hohmann & E. Klipp, (2010) Biophysical properties of

Saccharomyces cerevisiae and their relationship with HOG pathway activation. *Eur Biophys J* **39**: 1547-1556.
Vindelov, J. & N. Arneborg, (2002) Saccharomyces cerevisiae and Zygosaccharomyces mellis exhibit different hyperosmotic shock responses. *Yeast* **19**: 429-439.

Table S6: Reaction rate constants and model parameters.

$[]_0$ indicates initial concentration (µmol/l). The volume is in litre (l), and the concentration is µmol/l, mass is in grams and time in seconds.

Parameter	Value	Description	Method
k_1	0.00275	As^{III} Influx-efflux rate through Fps1 channel.	Estimated
k_2	0.00876	As^{III} -Protein binding rate constant.	Estimated
k_3	0.000645	As^{III}_{prot} dissociation rate constant.	Estimated
k_4	0.063925	As^{III} induced Hog1 phosphorylation rate constant.	Estimated
k_5	118.09	Dual phosphorylated Hog1, dephosphorylation rate constant.	Estimated
$k_{6\text{-}As^{III}}$	0.00018	As^{III} induced Fps1 phosphorylation rate constant.	Estimated
$k_{6\text{-}Hog1}$	853.5	Hog1 induced Fps1 phosphorylation rate constant.	Estimated
$k_{6\text{-}basal}$	0.051	Basal Fps1 phosphorylation rate constant.	Estimated
k_7	0.0501	Phosphorylated Fps1, dephosphorylation rate constant.	Estimated
k_8	0.8665	As^{III} -glutathione conjugation rate constant.	Estimated
k_9	19.93	$As(GS)_3$ dissociation rate constant.	Estimated
k_{10}	4.2e-06	Vacuolar sequestration of $As(GS)_3$ rate constant.	Estimated
k_{11}	2.4e-07	$vAs(GS)_3$ vacuolar export rate constant.	Estimated
k_{12}	$\frac{k_{13} \cdot [Acr3]_0}{[As^{III}_{in}]_0}$	Acr3 expression rate constant which is calculated.	Calculated
k_{13}	1e-8	Acr3 degradation rate constant.	Estimated
k_{m14}	5.2e-06	Acr3 mediated As^{III} export michaelis-constant.	Estimated
V_{m14}	1	Acr3 mediated, maximum As^{III} export rate constant.	Set
$As^{III}_{in\text{-}ACR3^+}$	20.413	Initial concentration of free intracellular arsenite in $ACR3^+$ mutants and WT.	Estimated
$Fps1P_{max}$	0.03	Maximum phosphorylated Fps1 estimated from data.	Estimated

Δ[Ycf1]	15.622	Ycf1 increase in *acr3Δ* mutants relative to wild type cells.	Estimated
$[(GSH)_3]_{r\text{-}acr3\Delta hog1\Delta}$	6.9888	Initial glutathione increase, in *acr3Δhog1Δ* mutant relative to wild type.	Estimated
$[(GSH)_3]_{r\text{-}acr3\Delta}$	3.28633	Initial glutathione increase in *acr3Δ* and *acr3Δycf1Δ* mutants relative to wild type.	Estimated

Reference:

Table S7: Fps1 and Hog1 phosphorylation data

Phosphorylated Fps1 was measured using western-blot for wild type and *hog1Δ* mutant. In addition, phosphorylated Hog1 was measured up to 60 minutes after 1mM As^{III} stress. The data are derived from Thorsen *et al.(Thorsen et al., 2006)*.

% phosphoFPS1 Control		**% phosphoFPS1 upon 1.0 mM As^{III} stress**	
WT	**hog1Δ**	**WT+As**	**hog1Δ+As**
24.8	16.2	45.6	39.6
30.1	27.3	35.8	28.8
28.3	23.5	34.5	24.1
26.1	23.6	30.1	25.4
16.5	15	38.4	29.9
29.4	20.1	49.9	33.4
17.9	10	39.1	38.8
22.3	18.7	35.5	32.1
16	13		
14	10		
17	13		

Time	**% Hog1PP upon 1.0 mM As^{III} stress in wild type**
0	3.2
15	7.7
30	6.5
60	6.8

Thorsen, M., Y. Di, C. Tangemo, M. Morillas, D. Ahmadpour, C. Van der Does, A. Wagner, E. Johansson, J. Boman, F. Posas, R. Wysocki & M.J. Tamas, (2006) The MAPK Hog1p modulates Fps1p-dependent arsenite uptake and tolerance in yeast. *Mol Biol Cell* **17**: 4400-4410.